Monthly Notices
of the
ROYAL ASTRONOMICAL SOCIETY

Mon. Not. R. Astron. Soc. **425,** 2128–2143 (2012) doi:10.1111/j.1365-2966.2012.21567.x

Redshift-space distortions in $f(R)$ gravity

Elise Jennings,[1,2]⋆ Carlton M. Baugh,[3] Baojiu Li,[3] Gong-Bo Zhao[4,5] and Kazuya Koyama[4]

[1] *The Kavli Institute for Cosmological Physics, University of Chicago, 5640 South Ellis Avenue, Chicago, IL 60637, USA*
[2] *The Enrico Fermi Institute, University of Chicago, 5640 South Ellis Avenue, Chicago, IL 60637, USA*
[3] *Institute of Computational Cosmology, Department of Physics, Durham University, South Road, Durham DH1 3LE*
[4] *Institute of Cosmology & Gravitation, University of Portsmouth, Portsmouth PO1 3FX*
[5] *National Astronomy Observatories, Chinese Academy of Science, Beijing 100012, China*

Accepted 2012 June 19. Received 2012 June 14; in original form 2012 May 11

ABSTRACT

We use large-volume N-body simulations to predict the clustering of dark matter in redshift space in $f(R)$ modified gravity cosmologies. This is the first time that the non-linear matter and velocity fields have been resolved to such a high level of accuracy over a broad range of scales in this class of models. We find significant deviations from the clustering signal in standard gravity, with an enhanced boost in power on large scales and stronger damping on small scales in the $f(R)$ models compared to general relativity (GR) at redshifts $z < 1$. We measure the velocity divergence ($P_{\theta\theta}$) and matter ($P_{\delta\delta}$) power spectra and find a large deviation in the ratios $\sqrt{P_{\theta\theta}/P_{\delta\delta}}$ and $P_{\delta\theta}/P_{\delta\delta}$ between the $f(R)$ models and GR for $0.03 < k/(h\,\mathrm{Mpc}^{-1}) < 0.5$. In linear theory, these ratios equal the growth rate of structure on large scales. Our results show that the simulated ratios agree with the growth rate for each cosmology (which is scale-dependent in the case of modified gravity) only for extremely large scales, $k < 0.06\,h\,\mathrm{Mpc}^{-1}$ at $z = 0$. The velocity power spectrum is substantially different in the $f(R)$ models compared to GR, suggesting that this observable is a sensitive probe of modified gravity. We demonstrate how to extract the matter and velocity power spectra from the 2D redshift-space power spectrum, $P(k, \mu)$, and can recover the non-linear matter power spectrum to within a few per cent for $k < 0.1\,h\,\mathrm{Mpc}^{-1}$. However, the model fails to describe the shape of the 2D power spectrum, demonstrating that an improved model is necessary in order to reconstruct the velocity power spectrum accurately. The same model can match the monopole moment to within 3 per cent for GR and 10 per cent for the $f(R)$ cosmology at $k < 0.2\,h\,\mathrm{Mpc}^{-1}$ at $z = 1$. Our results suggest that the extraction of the velocity power spectrum from future galaxy surveys is a promising method to constrain deviations from GR.

Key words: cosmology: theory – dark energy – large-scale structure of Universe.

1 INTRODUCTION

The clustering of galaxies on different scales is a key observational tool in the quest to explain the current accelerating expansion of the Universe (Percival et al. 2007; Schlegel et al. 2007, 2009; Guzzo et al. 2008; LSST Science Collaborations 2009; Blake et al. 2010, 2011; Sánchez et al. 2010; Beutler et al. 2011; Green et al. 2011; Laureijs et al. 2011; Blake et al. 2012). The accelerating expansion may be the result of a dark energy component which behaves as a repulsive form of gravity or it may be that Einstein's theory of gravity breaks down on cosmological scales (see e.g. Bertschinger & Zukin 2008; Weinberg et al. 2012). For a given cosmology with a smooth dark energy component, a measurement of the expansion history gives a prediction for the growth rate of structure. Independent measurements of the growth rate can be obtained by measuring the clustering of galaxies in redshift space, where peculiar velocities distort the clustering signal along the line of sight. By testing the consistency between the measured growth rate and the prediction from the expansion history, it is possible to constrain models of modified gravity and to distinguish them from a smooth dark energy component (see e.g. Mortonson et al. 2009; Vanderveld et al. 2012). In this paper we measure the anisotropic power spectrum in redshift space from large-volume N-body simulations of $f(R)$ modified gravity and general relativity (GR) cosmologies.

The $f(R)$ class of models can mimic the effect of a cosmological constant and is set up by modifying the Einstein–Hilbert action with an arbitrary function of the Ricci scalar, R (see e.g. Carroll et al.

⋆E-mail: ejennings@kicp.uchicago.edu

2003; Nojri & Odintsov 2003). A key feature of these models is the existence of a 'fifth force', due to an extra propagating scalar field. Departures from GR on small scales are highly constrained by Solar system tests (e.g. Will 2006). As a result, viable $f(R)$ theories must exhibit a screening mechanism, the so-called chameleon effect (Khoury & Weltman 2004), whereby standard gravity is recovered in high-density environments. The range of the fifth force depends non-linearly on the local curvature and as a result will change with redshift. The impact of the chameleon mechanism on the matter and velocity fields can only be fully investigated using N-body simulations. Any deviations from standard gravity will depend on the choice of the function $f(R)$ and the parameter values adopted.

In this paper we consider the $f(R)$ model proposed by Hu & Sawicki (2007). This modified gravity model has been incorporated into N-body simulations and studied by several authors (Oyaizu 2008; Oyaizu, Lima & Hu 2008; Schmidt, Vikhlinin & Hu 2009a; Schmidt et al. 2009b; Ferraro, Schmidt & Hu 2010; Lombriser et al. 2010; Gil-Marín et al. 2011; Li & Hu 2011; Zhao, Li & Koyama 2011). A variety of computational box sizes from 64 to 400 Mpc h^{-1} on a side have been used. In this work we make use of large-volume, $L_{\rm box} = 1.5$ and 1 Gpc h^{-1}, modified gravity simulations using the N-body code of Li et al. (2012). The large volume of these simulations allow us to study the impact of unique features of modified gravity, such as the scale-dependent enhanced gravitational force, on the clustering signal in redshift space.

Galaxy redshift surveys allow us to study the 3D spatial distribution of galaxies and clusters. In addition to the Hubble flow, galaxies have peculiar velocities, due to local inhomogeneities in the density field, which distort the measured distances. Measuring the anisotropic distortions in the galaxy clustering pattern in redshift-space constrains $\beta = f/b$, where b is the galaxy bias factor and f is the logarithmic derivative of the linear growth rate of structure, which is scale-independent in the case of GR. This effect was first described by Kaiser (1987) using linear perturbation theory where the matter power spectrum in redshift space can be expressed as a function of the power spectrum in real space and β. Several authors have extended this linear model to quasi-linear scales by, for example, including non-linear velocity terms (Scoccimarro 2004; Matsubara 2008; Percival & White 2009; Taruya, Nishimichi & Saito 2010) or by considering a phase-space distribution function approach (Seljak & McDonald 2011) or into the non-linear regime by including the contribution of peculiar velocities on small scales (e.g. Peebles 1976; Peacock & Dodds 1994; Reid & White 2011).

Modelling the clustering of the dark matter and galaxies in redshift space is extremely challenging. Most models contain free parameters such as the linear bias, which quantifies the difference in clustering between the dark matter and galaxies on large scales, and the velocity dispersion due to incoherent motions on small scales (see e.g. Okumura & Jing 2011). These parameters must be included when fitting any model and can weaken the constraints on the growth rate.

Many redshift-space distortion models which are currently used are only accurate for a limited range of scales or for galaxies with a particular linear bias (e.g. Scoccimarro 2004; Reid & White 2011). Scoccimarro (2004) proposed a simple quasi-linear model which includes the non-linear velocity power spectrum. By comparing with measurements from N-body simulations, Jennings, Baugh & Pascoli (2011a,b) showed that this model performed better than commonly used models (which we discuss in Section 3) and is accurate on scales $k < 0.3\,h$ Mpc^{-1} and can recover the linear growth rate to within a few per cent. The non-linear velocity terms in this model may be obtained either using a fitting formula calibrated against N-body simulations or from perturbation theory (Matsubara 2008; Jennings et al. 2011a).

The WiggleZ Dark Energy Survey (Blake et al. 2011) recently measured the growth rate at $z = 0.78$ to be $f = 0.70 \pm 0.08$ using redshift-space distortions in the galaxy power spectrum. Measurements of the linear growth rate are degenerate with the bias or clustering amplitude in the power spectra and so constraints on the growth rate are often quoted as constraints on $f\sigma_8$, where σ_8 is the rms variance in the linear matter power spectra smoothed in spheres of radius 8 Mpc h^{-1} (Percival & White 2009). The 6dF Galaxy Survey modelled the 2D galaxy correlation function and obtained a low-redshift measurement of the growth rate, $f\sigma_8 = 0.423 \pm 0.055$, at an effective redshift of $z = 0.067$ (Beutler et al. 2012). Recent measurements from the Third Sloan Digital Sky Survey (SDSS-III) BOSS survey found $\mathrm{d}\sigma_8/\mathrm{d}\ln a = 0.43 \pm 0.069$ at an effective redshift of $z = 0.57$ (Reid et al. 2012). All of these results are consistent with the Λ cold dark matter (ΛCDM) model and standard gravity. Current surveys do not have sufficient precision to rule out viable modified gravity models such as the $f(R)$ models considered in this paper. Future galaxy redshift surveys, such as the ESA's *Euclid* mission (Laureijs et al. 2011) and the ground-based stage IV dark energy experiment, BigBOSS (Schlegel et al. 2009), aim to measure the growth rate to within 2 per cent, which will place significant constraints on currently allowed modified gravity models.

A key feature of redshift-space distortion models is that the linear growth rate is assumed to be scale-independent. This assumption is not true for the modified gravity cosmology considered in this paper (see Fig. 1). In addition, several models of redshift-space distortions suffer from systematic biases when fitting for a scale-independent growth rate over a range of scales (see fig. 5 in Jennings et al. 2011b). In order to avoid assuming a specific scale dependence for the growth rate, we instead focus on recovering the velocity and matter power spectra as a function of scale using the full 2D redshift-space power spectrum. This approach makes use of the full 2D power spectrum measured from a survey, and the extracted matter and velocity power spectra could be compared to predictions from the standard cosmological model.

In this paper we measure the power spectrum in redshift space from a suite of large-volume simulations of $f(R)$ cosmologies (Li et al. 2012). This is the first time that predictions for the

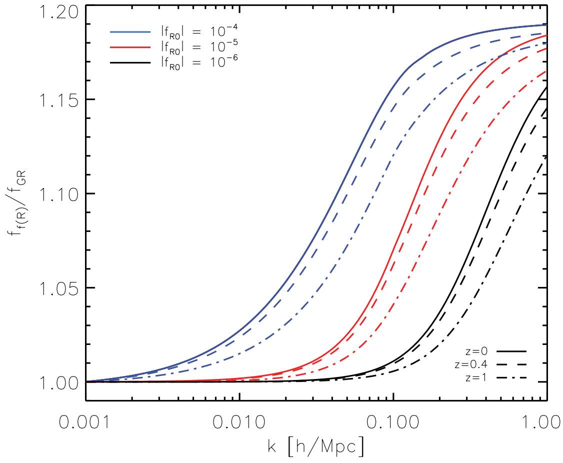

Figure 1. The ratio of the linear growth rate in the F4 (blue), F5 (red) and F6 (black) cosmologies to that in ΛCDM. The ratios are shown at $z = 0$ (solid), $z = 0.4$ (dashed) and $z = 1$ (dot–dashed). (See Section 2.2 for the description of the modified gravity models.)

redshift-space clustering in $f(R)$ modified gravity models have been presented. The resolution of our simulations allows us to accurately resolve the non-linear matter and velocity fields and quantify the deviations from a model of GR. Here, we restrict our study to the clustering of the dark matter. We examine the difference between the velocity power spectra in each cosmology and its importance in modelling the redshift-space clustering signal in both the standard and modified gravity model. We test how well quasi-linear models for the redshift-space distortions describe the amplitude and shape of the measured power spectrum. A follow-up paper will examine the redshift-space distortions in the clustering of haloes as well as testing non-linear models for redshift-space distortions (see also e.g. Marulli et al. 2012, for a recent study of redshift-space distortions in interacting dark energy models).

This paper is organized as follows. In Section 2.1 we discuss the $f(R)$ modified gravity cosmological model and describe the N-body simulations used in this paper. In Section 3 we review the theory of redshift-space distortions and present the models which will be tested. The main results of the paper are presented in Section 4. Measurements of the redshift-space power spectra for both GR and $f(R)$ models are presented in Section 4.1. In Section 4.2 we present the velocity power spectrum measured from the simulations. Using a quasi-linear model for the redshift-space power spectrum we attempt to extract both the matter and velocity power spectra from the 2D redshift-space power spectrum in Section 4.3. In Section 4.4 we examine how well the moments of the redshift-space power spectrum can be recovered using this quasi-linear model. Our conclusions are presented in Section 5. Throughout the paper we shall use the unit $c = 1$ and metric convention $(+, -, -, -)$. Greek letters $\mu, \nu, \ldots$ run over 0, 1, 2, 3 and Latin letters $i, j, k, \ldots$ run over 1, 2, 3.

2 $f(R)$ COSMOLOGIES

This section gives the theoretical background for the modified gravity model considered in this paper. We outline $f(R)$ cosmologies in Section 2.1, explain the chameleon mechanism in Section 2.2 and describe the N-body code and simulations in Section 2.3.

2.1 The $f(R)$ gravity model

The $f(R)$ gravity model is a straightforward generalization of GR: the Ricci scalar, R, in the Einstein–Hilbert action, S, is replaced with an algebraic function, $f(R)$ (see e.g. De Felice & Tsujikawa 2010; Sotiriou & Faraoni 2010, for recent reviews):

$$S = \int \mathrm{d}^4x\sqrt{-g}\left\{\frac{M_{\rm Pl}^2}{2}\left[R + f(R)\right] + \mathcal{L}_{\rm m}\right\}, \tag{1}$$

where $M_{\rm Pl}$ is the Planck mass, $M_{\rm Pl}^{-2} = 8\pi G$, with G being Newton's constant, g is the determinant of the metric $g_{\mu\nu}$ and $\mathcal{L}_{\rm m}$ is the Lagrangian density for matter fields (photons, neutrinos, baryons and CDM). By specifying the functional form of $f(R)$, one specifies the $f(R)$ gravity model.

Varying the action defined in equation (1) with respect to the metric $g_{\mu\nu}$ yields the modified Einstein equation

$$G_{\mu\nu} + f_R R_{\mu\nu} - \left(\frac{1}{2}f - \Box f_R\right) g_{\mu\nu} - \nabla_\mu\nabla_\nu f_R = 8\pi G T^{\rm m}_{\mu\nu}, \tag{2}$$

where $G_{\mu\nu} \equiv R_{\mu\nu} - \frac{1}{2}g_{\mu\nu}R$ is the Einstein tensor, $f_R \equiv \mathrm{d}f/\mathrm{d}R$, ∇_μ is the covariant derivative compatible with the metric $g_{\mu\nu}$, $\Box \equiv \nabla^\alpha\nabla_\alpha$ and $T^{\rm m}_{\mu\nu}$ is the energy momentum tensor for matter. One can consider equation (2) as a fourth-order differential equation, or alternatively the standard second-order equation of GR with a new dynamical degree of freedom, f_R, the equation of motion of which can be obtained by taking the trace of equation (2):

$$\Box f_R = \frac{1}{3}\left(R - f_R R + 2f + 8\pi G\rho_{\rm m}\right), \tag{3}$$

where $\rho_{\rm m}$ is the matter density. The new degree of freedom f_R is sometimes dubbed the *scalaron* in the literature.

Assuming that the background Universe is described by the flat Friedmann–Robertson–Walker metric, the line element in the perturbed Universe is written as

$$\mathrm{d}s^2 = a^2(\eta)\left[(1 + 2\Phi)\,\mathrm{d}\eta^2 - (1 - 2\Psi)\,\mathrm{d}x^i\,\mathrm{d}x_i\right], \tag{4}$$

where η and x^i are, respectively, the conformal time and comoving coordinates, $\Phi(\eta, \boldsymbol{x})$ and $\Psi(\eta, \boldsymbol{x})$ are the Newtonian potential and perturbation to the spatial curvature, and are functions of both time (η) and space ($\boldsymbol{x}$); a denotes the scale factor of the Universe where $a = 1$ today.

As we are mainly interested in the large-scale structures much smaller than the Hubble scale, and since the time variation of f_R is very small in the models considered below, we shall work in the quasi-static limit by neglecting the time derivatives of f_R. In this limit, the scalaron equation, equation (2), reduces to

$$\vec{\nabla}^2 f_R = -\frac{1}{3}a^2\left[R(f_R) - \bar{R} + 8\pi G\left(\rho_{\rm m} - \bar{\rho}_{\rm m}\right)\right], \tag{5}$$

where $\vec{\nabla}$ is the 3D gradient operator (to be distinguished from the ∇ introduced above) and the overbar represents the background value of a quantity. Note that R can be expressed as a function of f_R.

Similarly, the Poisson equation which governs the Newtonian potential, Φ, can be simplified to

$$\vec{\nabla}^2\Phi = \frac{16\pi G}{3}a^2\left(\rho_{\rm m} - \bar{\rho}_{\rm m}\right) + \frac{1}{6}a^2\left[R\left(f_R\right) - \bar{R}\right] \tag{6}$$

by neglecting terms involving time derivatives and using equation (5) to eliminate $\vec{\nabla}^2 f_R$.

According to the above equations, there are two potential effects of the scalaron on cosmology: (i) the background expansion of the Universe may be modified by the new terms in equation (2) and (ii) the relationship between gravity and the matter density field is modified, which can change the matter clustering and growth of density perturbations. Clearly, when $|f_R| \ll 1$, we have $R \approx -8\pi G\rho_{\rm m}$ from equation (5), and so equation (6) reduces to the normal Poisson equation in GR; when $|f_R|$ is large, we instead have $|R - \bar{R}| \ll 8\pi G|\rho_{\rm m} - \bar{\rho}_{\rm m}|$, and so equation (6) reduces to the normal Poisson equation with G rescaled by 4/3. Note that this factor of 4/3 is the maximum enhancement of gravity in $f(R)$ models, independent of the specific functional form of $f(R)$. The choice of $f(R)$, however, is important because it governs when and on which scale the enhancement factor changes from unity to 4/3: scales much larger than the range of the modification to Newtonian gravity mediated by the scalaron are unaffected and gravity is not enhanced there, while on much smaller scales the 4/3 enhancement is fully realized – this results in a scale-dependent modification of gravity and therefore a scale-dependent growth rate of structure (see Fig. 1).

The relationship between Φ and Ψ is also changed in $f(R)$ models, with the remaining components of the modified Einstein equation giving

$$\vec{\nabla}^2(\Psi - \Phi) = \vec{\nabla}^2 f_R, \tag{7}$$

where we have assumed that $|\bar{f}_R| \ll 1$. This implies that

$$\vec{\nabla}^2(\Phi + \Psi) = 8\pi G\left(\rho_{\rm m} - \bar{\rho}_{\rm m}\right)a^2. \tag{8}$$

Therefore, the relationship between the lensing potential and the matter density perturbations remains unchanged in $f(R)$ gravity models.

2.2 The chameleon mechanism

The $f(R)$ gravity would be ruled out by local tests of gravity due to the factor of 4/3 enhancement to the strength of Newtonian gravity. Fortunately, it is well known that, if $f(R)$ is chosen appropriately, the chameleon mechanism (Khoury & Weltman 2004; Mota & Shaw 2007) can be exploited to suppress the enhancement allowing this class of models to satisfy experimental constraints in high matter density regions such as in our Solar system (Hu & Sawicki 2007; Li & Barrow 2007; Navarro & Van Acoleyen 2007; Brax et al. 2008).

The essence of the chameleon mechanism is as follows. The modifications to the Newtonian gravity can be considered as an extra, or the fifth force mediated by the scalaron. Because the scalaron itself is massive, the force is of the Yukawa type and is suppressed by the exponential factor $\sim\exp(-mr)$, in which m is the scalaron mass and r the distance between two test masses. In high matter density environments, m is very heavy and the suppression becomes very strong. In practice, this is equivalent to the fact that $|f_R| \ll 1$ in high-density regions because of the exponential suppression, which leads to the GR limit as discussed above.

As a result, the functional form of $f(R)$ is crucial to determine whether the fifth force is sufficiently suppressed in high-density environments. In this work we study the $f(R)$ model proposed by Hu & Sawicki (2007), for which

$$f(R) = -M^2\frac{c_1(-R/M^2)^n}{c_2(-R/M^2)^n+1}, \tag{9}$$

with $M^2 \equiv 8\pi G\bar{\rho}_{\mathrm{m}0}/3 = H_0^2\Omega_{\mathrm{m}}$, where H is the Hubble expansion rate and Ω_{m} is the present-day fractional density of matter. Hereafter a subscript 0 always means the current value of a quantity. Hu & Sawicki (2007) demonstrated that $|f_{R0}| < 0.1$ is required for this model to evade Solar system constraints, although the exact value also depends on the behaviour of f_R in the Galaxy.

In the background cosmology, the scalaron f_R always sits at the minimum of the effective potential which governs its dynamics, defined as

$$V_{\mathrm{eff}}(f_R) \equiv \frac{1}{3}\left(R - f_R R + 2R + 8\pi G\rho_{\mathrm{m}}\right), \tag{10}$$

around which it oscillates quickly (Brax et al. 2012). Therefore, we have

$$-\bar{R} \approx 8\pi G\bar{\rho}_{\mathrm{m}} - 2\bar{f} = 3M^2\left(a^{-3} + \frac{2c_1}{3c_2}\right). \tag{11}$$

To match the ΛCDM background evolution, we need to have

$$\frac{c_1}{c_2} = 6\frac{\Omega_\Lambda}{\Omega_{\mathrm{m}}}, \tag{12}$$

where Ω_Λ is the current fractional energy density of the dark energy (cosmological constant).

By taking $\Omega_\Lambda \approx 0.76$ and $\Omega_{\mathrm{m}} \approx 0.24$, we find that $|\bar{R}| \approx 41M^2 \gg M^2$, and this simplifies the expression of the scalaron to

$$f_R \approx -n\frac{c_1}{c_2^2}\left(\frac{M^2}{-R}\right)^{n+1}. \tag{13}$$

Therefore, two free parameters, n and c_1/c_2^2, completely specify the $f(R)$ model. Indeed, the latter is related to the value of the scalaron today, f_{R0}, as

$$\frac{c_1}{c_2^2} = -\frac{1}{n}\left[3\left(1+4\frac{\Omega_\Lambda}{\Omega_{\mathrm{m}}}\right)\right]^{n+1} f_{R0}. \tag{14}$$

In what follows we shall study three $f(R)$ models with $n = 1$ and $|f_{R0}| = 10^{-6}, 10^{-5}$ and 10^{-4}, which will hereafter be referred to as F6, F5 and F4, respectively. These particular parameter choices arise from cluster abundance constraints on the $f(R)$ gravity model. The current constraint found by Schmidt et al. (2009a) is $|f_{R0}| < 1.3^{+1.7}_{-0.6} \times 10^{-4}$ taking into account mass calibration errors.

2.3 *N*-body simulations of $f(R)$ gravity

From equations (5) and (6) we can see that, given the matter density field, we can solve for the scalaron field, f_R, from equation (5) and plug this into the modified Poisson equation (6) to solve for Φ. Once Φ is at hand, we can difference it to calculate the (modified) gravitational force which determines how the particles move subsequently. This is exactly what we need to do in *N*-body simulations to follow the evolution of the matter distribution.

The main challenge in the *N*-body simulation of models such as $f(R)$ gravity is to solve the scalaron equation, equation (5), which is in general very non-linear. For this we need a mesh (or a set of meshes) on which f_R can be solved. This implies that mesh-based *N*-body codes are the most suitable for this task. On the other hand, particle-based codes are more difficult to apply in this case, as we do not have an analytical formula for the modified force law (i.e. the equivalent of r^{-2} in the Newtonian case).

N-body simulations for $f(R)$ gravity and related theories have been performed by Oyaizu (2008), Oyaizu et al. (2008), Schmidt et al. (2009b), Zhao et al. (2011), Li & Zhao (2009, 2010), Schmidt (2009), Li & Barrow (2011), Brax et al. (2011) and Davis et al. (2012). However, these simulations were affected by the small box size used and the limited resolution. For this work we have run simulations of $f(R)$ cosmologies using the recently developed ECOSMOG code (Li et al. 2012). ECOSMOG is a modification of the mesh-based *N*-body code RAMSES (Teyssier 2002), which calculates the gravitational force by first solving the Poisson equation on meshes using a relaxation method to get the Newtonian potential and then differencing the potential; it does not solve gravity by summing over the forces from nearby particles as is done, for example, in the simulation code GADGET (Springel 2005). Additional features of the ECOSMOG code include the following.

(i) The adaptive mesh refinement (AMR), which refines a mesh cell, i.e. splits it into eight son cells, if the number of particles in a cell exceeds a pre-defined number (the refinement criterion). As such it gives higher force resolution in high matter density regions where the chameleon effect is strong and the $f(R)$ equation is more non-linear. The refinement criterion is normally chosen as a particle number between 8 and 12, and in our simulations we adopt a condition of nine particles. This adaptive mesh allows us to reach comparable spatial resolution to codes like GADGET.

(ii) The multigrid relaxation algorithm that ensures quick convergence. The relaxation method finds the solution to an elliptical partial differential equation (PDE) on a mesh by iteratively updating the initial guess until it converges, i.e. becomes close enough to the true solution. However, the rate of convergence slows down quickly after the first few iterations. To improve on this, one can ‘coarsify’ the PDE, i.e. move it to a coarser mesh, solve it there and use the coarse solution to improve the solution on the original fine mesh. Unlike other codes, ECOSMOG does this on all the AMR meshes, greatly improving the convergence properties of the whole code.

(iii) The massive parallelization which makes the computation very efficient. This is the key feature that enables us to run large

Table 1. Some technical details of the simulations performed in this work. F6, F5 and F4 are, respectively, the abbreviations which denote the $f(R)$ models with $|f_{R0}| = 10^{-6}, 10^{-5}$ and 10^{-4}. For all models we have assumed $\Omega_{\rm m} = 0.24$ and $\Omega_\Lambda = 0.76$, and to generate the initial conditions we have used $\sigma_8 = 0.769$ (in agreement with e.g. Sánchez et al. 2009). We use the same initial conditions for all models in each simulation, because at the initial time, $z_{\rm i} = 49$, the difference in the power spectra of different models is negligible. ϵ is the residual for the Gauss–Seidel relaxation used in the code (see Li et al. 2012), and the two values of the convergence criterion are for the coarsest level and finest levels, respectively. Other cosmological parameters are a Hubble constant of $H_0 = 73\,{\rm km\,s^{-1}\,Mpc^{-1}}$ and a scalar spectral index of $n = 0.961$.

Models	$L_{\rm box}$ (h^{-1} Gpc)	Particles	Domain meshes	Finest meshes	Convergence criterion	Realizations
ΛCDM, F6, F5, F4	1.0	1024^3	1024^3	65536^3	$\|\epsilon\| < 10^{-12}/10^{-8}$	1
ΛCDM, F6, F5, F4	1.5	1024^3	1024^3	65536^3	$\|\epsilon\| < 10^{-12}/10^{-8}$	6

simulations such as the ones to be described below, which are beyond the reach of any serial code, such as those developed by Li & Zhao (2009, 2010) and Li & Barrow (2011).

A convergence criterion is used to determine when the relaxation method has converged. In ECOSMOG, convergence is considered to be achieved when the residual of the PDE, i.e. the difference between the two sides of the PDE, is smaller than a pre-defined parameter ϵ. We have checked that for $\epsilon < 10^{-8}$, the solution to the PDE no longer changes significantly when ϵ is reduced further. Our choices of ϵ are listed in Table 1. The computational time depends on both the value of ϵ and the model. The $f(R)$ gravity simulations can take a few times longer to run than the GR simulation. More details can be found in Li et al. (2012).

For the study of redshift-space distortions, large simulation boxes are essential to accurately model behaviour on very large scales. For this reason, we have run two sets of simulations, with $L_{\rm box} = 1.0$ and $1.5\,h^{-1}$ Gpc, respectively. The initial conditions are generated at $z = 49$ using the MPGRAFIC[1] code, and each suite of F4/F5/F6/GR simulations uses the same initial conditions because at $z = 49$ the difference in the matter distribution in the different cosmologies is negligible. The specifications of the simulations are summarized in Table 1.

3 MODELS FOR REDSHIFT-SPACE DISTORTIONS

In this section we first review the linear perturbation theory of redshift-space distortions (Section 3.1) before outlining some extended models which go beyond linear theory (Section 3.2).

3.1 Linear theory

Inhomogeneous structure in the universe induces peculiar motions which distort the clustering pattern measured in redshift space on all scales. This effect must be taken into account when analysing 3D data sets which use redshift to estimate the radial coordinate. Redshift-space effects alter the appearance of the clustering of matter, and together with non-linear evolution and bias, lead the measured power spectrum to depart from the simple predictions of linear perturbation theory. The comoving distance to a galaxy, $\boldsymbol{s}$, differs from its true distance, $\boldsymbol{x}$, due to its peculiar velocity, $\boldsymbol{v}(\boldsymbol{x})$ (i.e. an additional velocity to the Hubble flow). The mapping from redshift space to real space is given by

$$\boldsymbol{s} = \boldsymbol{x} + u_z\hat{z}, \tag{15}$$

where $u_z = \boldsymbol{v}\cdot\hat{z}/(aH)$ and $H(a)$ is the Hubble parameter. This assumes that the distortions take place along the line of sight denoted by $\hat{z}$ (this is the plane-parallel approximation). This assumption will break down for some pairs of galaxies in a survey which has a wide field of view (Raccanelli, Samushia & Percival 2010). Nevertheless, the impact of this systematic on clustering statistics has been shown to be small in comparison to the effects of non-linear growth (Samushia, Percival & Raccanelli 2012).

On small scales, randomized velocities associated with the motion of galaxies inside virialized structures reduce the power. The dense central regions of galaxy clusters appear elongated along the line of sight in redshift space, which produces the ‘fingers of God’ effect in redshift survey cone plots (Jackson 1972). On large scales, coherent bulk flows distort clustering statistics (see Hamilton 1998, for a review of redshift-space distortions). For growing perturbations on large scales, the overall effect of redshift-space distortions is to enhance the clustering amplitude. Any difference in the velocity field due to mass flowing from underdense regions to high-density regions will alter the volume element, causing an enhancement of the apparent density contrast in redshift space, $\delta_s(\boldsymbol{k})$, compared to that in real space, $\delta_r(\boldsymbol{k})$. This effect was first analysed by Kaiser (1987) in linear perturbation theory and can be approximated by

$$\delta_s(k) = \delta_r(k)(1 + \mu^2\beta), \tag{16}$$

where μ is the cosine of the angle between the wave vector, $\boldsymbol{k}$, and the line of sight, $\beta = f/b$, where f is the linear growth rate and the bias $b = 1$ for dark matter.

The ‘Kaiser formula’ (equation 16) relates the overdensity in redshift space to the corresponding value in real space and is the result of several approximations, e.g. that the velocity and density perturbations satisfy the linear continuity equation,

$$\delta = -f\theta, \tag{17}$$

where $\theta = \nabla\cdot\boldsymbol{u}$ is the velocity divergence. All of these assumptions are valid on scales that are well described by linear perturbation theory and will break down on different scales as the density fluctuations grow (see e.g. Jennings et al. 2011a, for more details). As shown in Scoccimarro (2004) and Jennings et al. (2011a), the linear regime corresponds to a different range of scales for the matter and velocity fields. In particular, linear theory is only a good description of the velocity power spectrum on surprisingly large scales. We will discuss this further in Section 4.2.

Rather than use the full 2D power spectrum, $P(k, \mu)$, it is common to decompose the matter power spectrum in redshift space into multipole moments using Legendre polynomials, $L_l(\mu)$ (see e.g. Hamilton 1998):

$$P(k,\mu) = \sum_l P_l(k)L_l(\mu)\,, \tag{18}$$

---

[1] http://www2.iap.fr/users/pichon/mpgrafic.html

where the summation is over the order, l, of the multipole. The anisotropy in $P(\boldsymbol{k})$ is symmetric in μ, as $P(k, \mu) = P(k, -\mu)$, so only even values of l are summed over. Each multipole moment is given by

$$P_l^s(k) = \frac{2l+1}{2} \int_{-1}^{1} P(k, \mu) L_l(\mu)\, \mathrm{d}\mu \,, \tag{19}$$

where the first two non-zero moments have Legendre polynomials, $L_0(\mu) = 1$ and $L_2(\mu) = (3\mu^2 - 1)/2$. Using the linear model in equation (16), the first three multipole moments are given by

$$\begin{pmatrix} P_0(k) \\ P_2(k) \\ P_4(k) \end{pmatrix} = P_{\delta\delta}(k) \begin{pmatrix} 1 + \frac{2}{3}\beta + \frac{1}{5}\beta^2 \\ \frac{4}{3}\beta + \frac{4}{7}\beta^2 \\ \frac{8}{35}\beta^2 \end{pmatrix} , \tag{20}$$

where $P_{\delta\delta}(k) = \langle|\delta(k)|^2\rangle$ denotes the real-space matter power spectrum. Note that we have neglected the superscript s here for clarity. In practice, $P_{\delta\delta}(k)$ cannot be obtained directly for a real survey without making approximations (e.g. Baugh & Efstathiou 1994).

In this paper we consider the estimator for β suggested by Cole, Fisher & Weinberg (1994), which is the ratio of the quadrupole to monopole moments of the redshift-space power spectrum, $P_2(k)/P_0(k)$, which is independent of the real-space power spectrum.

3.2 Quasi-linear and non-linear models for the redshift-space power spectrum

Assuming the line-of-sight component of the peculiar velocity is along the z-axis, the full non-linear relation between the real-space power spectrum and redshift-space power spectrum can be written as (Scoccimarro, Couchman & Frieman 1999)

$$P^s(k, \mu) = \int \frac{\mathrm{d}^3\boldsymbol{r}}{(2\pi)^3} \mathrm{e}^{-\mathrm{i}\boldsymbol{k}\cdot\boldsymbol{r}} \langle \mathrm{e}^{\mathrm{i}\lambda\Delta u_z}[\delta(\boldsymbol{x}) - \theta(\boldsymbol{x})][\delta(\boldsymbol{x}') - \theta(\boldsymbol{x}')]\rangle \,, \tag{21}$$

where $\lambda = k\mu$, u_z is the comoving peculiar velocity along the line of sight, $\Delta u_z = u_z(\boldsymbol{x}) - u_z(\boldsymbol{x}')$, $\boldsymbol{r} = \boldsymbol{x} - \boldsymbol{x}'$, $\theta = \nabla_z \cdot u_z$ and the only approximation made is the plane-parallel approximation. At small scales (as k increases), the exponential component damps the power, representing the impact of randomized velocities inside gravitationally bound structures.

Simplified models for redshift-space distortions are frequently used. Examples include multiplying equation (20) by a factor which attempts to take into account small-scale effects, invoking either a Gaussian or exponential distribution of peculiar velocities (Peacock & Dodds 1994). A popular phenomenological example of this which incorporates the damping effect of velocity dispersion on small scales is the so-called 'dispersion model' (Peacock & Dodds 1994):

$$P^s(k, \mu) = P^r(k)(1 + \beta\mu^2)^2 \frac{1}{1 + k^2\mu^2\sigma_\mathrm{p}^2/2} \,, \tag{22}$$

where σ_p is the pairwise velocity dispersion along the line of sight, which is treated as a parameter to be fitted to the data.

The linear model for the redshift-space power spectrum can be extended by keeping the non-linear velocity power spectra terms in equation (21). The velocity divergence autopower spectrum is the ensemble average, $P_{\theta\theta} = \langle|\theta|^2\rangle$, where $\theta = \nabla \cdot \boldsymbol{u}$ is the velocity divergence. The cross-power spectrum of the velocity divergence and matter density is $P_{\delta\theta} = \langle|\delta\theta|\rangle$. Scoccimarro (2004) proposed the following model for the redshift-space power spectrum in terms of $P_{\delta\delta}$, the non-linear matter power spectrum, $P_{\theta\theta}$ and $P_{\delta\theta}$:

$$P^s(k, \mu) = \left(P_{\delta\delta}(k) + 2\mu^2 P_{\delta\theta}(k) + \mu^4 P_{\theta\theta}(k)\right) \times \mathrm{e}^{-(k\mu\sigma_v)^2} \,, \tag{23}$$

where σ_v is the 1D linear velocity dispersion given by

$$\sigma_v^2 = \frac{1}{3} \int \frac{P_{\theta\theta}(k)}{k^2} \mathrm{d}^3k. \tag{24}$$

In linear theory, $P_{\theta\theta}$ and $P_{\delta\theta}$ take the same form as $P_{\delta\delta}$ and depart from this at different scales. Using a simulation with 512^3 particles in a box of length 479 h^{-1} Mpc (Yoshida, Sheth & Diaferio 2001), Scoccimarro (2004) showed that this simple ansatz for $P_s(k, \mu)$ was an improvement over the Kaiser formula when comparing to the results of N-body simulations in a ΛCDM cosmology.

In non-linear models for the power spectrum in redshift space, there is a degeneracy between the non-linear bias, the difference between the clustering of dark matter and haloes or galaxies, and the scale-dependent damping due to velocity distortions on small scales. This degeneracy will complicate any measurement of the growth rate using redshift-space clustering information on small scales. In addition these models assume that the growth rate is scale-independent, as is the case in GR. As shown in Fig. 1, the $f(R)$ model has scale-dependent growth rates which would have to be included when fitting any model to the measured redshift-space power spectrum.

In this paper we analyse the redshift-space clustering of the dark matter in $f(R)$ and ΛCDM cosmologies. We restrict our analysis to the linear and quasi-linear regime where the bias is typically assumed to be scale-independent and so our results can be more easily extended to linearly biased tracers of the dark matter field (but see Angulo, Baugh & Lacey 2008, for counterexamples). We will model the redshift-space distortions in the clustering of haloes in both of these cosmologies in future work.

We shall use the following model for the 2D redshift-space power spectrum,

$$P(k, \mu) = P_{\delta\delta}(k) + 2\mu^2 P_{\delta\theta}(k) + \mu^4 P_{\theta\theta}(k) \,, \tag{25}$$

where the first two multipole moments are given by

$$\begin{pmatrix} P_0(k) \\ P_2(k) \end{pmatrix} = \begin{pmatrix} 1 & \frac{2}{3} & \frac{1}{5} \\ 0 & \frac{4}{3} & \frac{4}{7} \end{pmatrix} \begin{pmatrix} P_{\delta\delta}(k) \\ P_{\delta\theta}(k) \\ P_{\theta\theta}(k) \end{pmatrix} . \tag{26}$$

This model has been shown to be a good fit to the power spectrum in redshift space measured from simulations at $z < 1$ (Jennings et al. 2011a,b).

4 RESULTS

In Section 4.1 we present measurements of the redshift-space power spectra for both GR and the $f(R)$ models. In Section 4.2 we present the velocity power spectrum measured from the simulations. We attempt to extract both the matter and velocity power spectra from the 2D redshift-space power spectrum using a quasi-linear model for the redshift space $P(k)$ in Section 4.3. In Section 4.4 we examine how well the moments of the redshift-space power spectrum can be recovered using this quasi-linear model.

4.1 The power spectrum in redshift space

In Figs 2 and 3 we plot the 2D power spectrum measured at $z = 0$ from the GR and F4 simulations and the F5 and F6 simulations, respectively, as a function of wavenumber perpendicular, k_perp, and parallel, k_para, to the line of sight. The colour contours

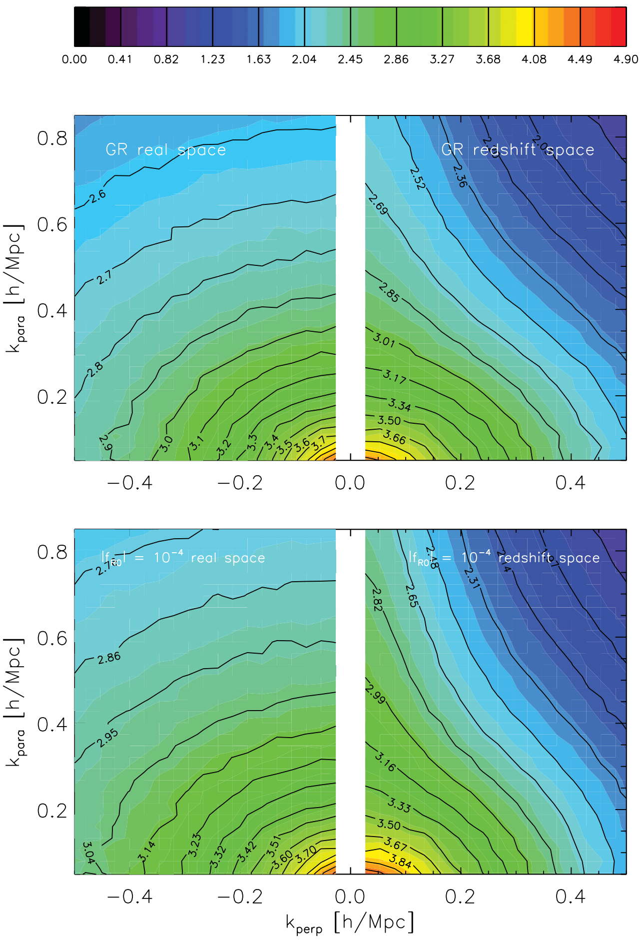

Figure 2. Top panels: the 2D power spectrum measured from the GR simulation as a function of wavenumber perpendicular, k_{perp}, and parallel, k_{para}, to the line of sight. The coloured shading and lines represent the amplitude of the power spectrum, $\log_{10}P$, as indicated by the labels and the scale bar at the top. The real-space power spectrum has been plotted at $k_{\mathrm{perp}} \rightarrow -k_{\mathrm{perp}}$ to allow comparison with the redshift space $P(k)$. Bottom panels: the 2D power spectrum measured from the F4 simulation as a function of modes perpendicular, k_{perp}, and parallel, k_{para}, to the line of sight.

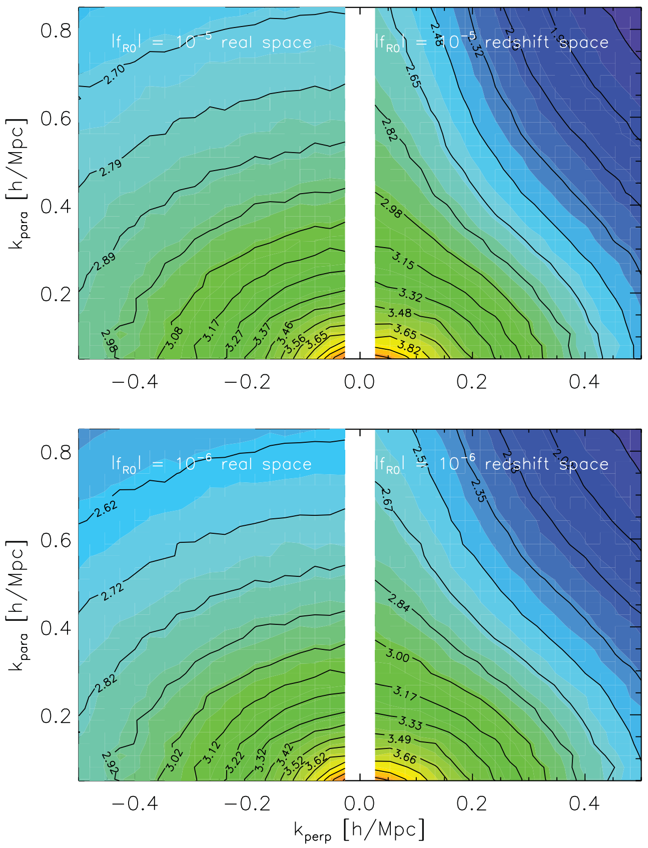

Figure 3. Top panels: the 2D power spectrum measured from the F5 simulation. Bottom panels: the 2D power spectrum measured from the F6 simulation. The coloured shading correspond to $\log_{10}P$ as shown in the colour bar in Fig. 2. As in Fig. 2, the left-hand panels show the power spectrum in real space and the right-hand panels show redshift space.

and lines represent the amplitude of the power spectrum, $\log_{10}P$. In each figure the real-space power spectrum has been plotted as $k_{\mathrm{perp}} \rightarrow -k_{\mathrm{perp}}$ in order to allow a side-by-side comparison with the redshift space $P(k)$. These figures clearly show that the spherical symmetry seen in the real-space power spectrum (left-hand panel) is distorted in redshift space (right-hand panel): on large scales ($k \rightarrow 0$), the amplitude of the redshift-space power spectrum is increased compared to that in real space, whereas on small scales, the power spectrum is damped and elongated along the line of sight in redshift space compared to real space. These effects were first convincingly observed in the clustering of galaxies measured by the 2dFGRS (Peacock et al. 2001) and again recently by the SDSS-III BOSS survey and the WiggleZ Dark Energy Survey [c.f. fig. 3 in Reid et al. (2012) and fig. 2 in Blake et al. (2011)]. These two effects are more pronounced in the F4 simulation where the large-scale boost and small-scale damping appear larger than in GR. Overall, the redshift space $P(k)$ for the $f(R)$ model appears far more distorted and asymmetrical than the corresponding redshift space $P(k)$ in GR.

In the left-hand panel of Fig. 4 we plot the ratio of the monopole of the redshift-space power spectrum to the real-space power spectrum at $z = 0$ measured from the GR (black) and F4 (blue) simulations. The right-hand panel of this figure shows the ratio of the quadrupole to monopole moment of the redshift-space power spectrum for both models at $z = 0$. The redshift-space power spectra are obtained from the simulations after averaging over the $P(k)$ obtained by treating the x, y and z directions in turn as the lines of sight. The errors on the ratios are plotted as a blue hatched region for the $f(R)$ cosmology and as a solid grey region for GR and represent the scatter amongst six realizations. Note that we have compared the errors obtained from six simulations to those from 10 simulations from Jennings et al. (2011b), which have the same box size and particle number, and find a 20 per cent decrease in the $z = 0$ error on the largest scale, $k \sim 0.01\,h\,\mathrm{Mpc}^{-1}$, when we use six simulations instead of 10. The linear theory predictions, given by equation (20), are shown as a green dot–dashed line for the $f(R)$ model and as a red dashed line for GR. These predictions use the linear growth rate for each model which for GR is $f(z = 0) = 0.42$ and is a scale-dependent factor, $f(k)$, for the $f(R)$ cosmology (see Fig. 1).

It is clear from Fig. 4 that the redshift-space power spectrum in the $f(R)$ model has a different shape compared to that in GR. First, there is an increased boost in the clustering signal on large scales, $k < 0.07\,h\,\mathrm{Mpc}^{-1}$, due to increased bulk flows into overdense regions seen in the modified gravity simulation. Nevertheless, the

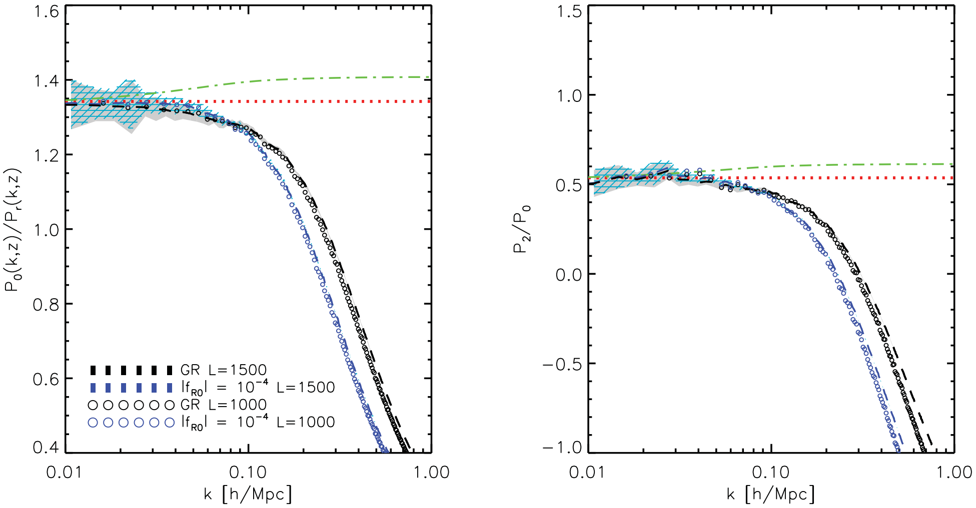

Figure 4. Left-hand panel: the ratio of the monopole of the redshift-space power spectrum to the real-space power spectrum at $z = 0$ in the F4 (blue) and GR (black) cosmologies. We plot the ratio measured from two simulation boxes: $L_{\mathrm{box}} = 1000\,\mathrm{Mpc}\,h^{-1}$ (circles) and $L_{\mathrm{box}} = 1500\,\mathrm{Mpc}\,h^{-1}$ (dashed lines). The linear theory prediction for each model is shown as a green dot–dashed line for the $f(R)$ model and as a red dashed line for GR. The shaded regions represent the errors on the ratios measured from six realizations of the $f(R)$ (blue hatched) and GR (grey solid) cosmologies. Right-hand panel: the ratio of the quadrupole to monopole moment of the redshift space $P(k)$ at $z = 0$ in the F4 (blue) and GR (black) cosmologies.

measurement from the simulation is significantly below the linear theory prediction for this cosmology. The small-scale damping due to incoherent motions within virialized structures is also more pronounced in the $f(R)$ cosmology compared to GR on scales $k > 0.1\,h\,\mathrm{Mpc}^{-1}$. It is clear from this plot that the linear perturbation theory limit is only attained on extremely large scales ($k < 0.02\,h\,\mathrm{Mpc}^{-1}$) for each model. On these scales the two models cannot be distinguished within the error bars. The large-scale boost in the redshift-space power spectrum in the $f(R)$ cosmology compared to GR is less pronounced in the quadrupole-to-monopole moment ratio plotted in the right-hand panel of Fig. 4. The increased damping of the redshift-space power spectrum found in the modified gravity model can again be seen on small scales ($k > 0.1\,h\,\mathrm{Mpc}^{-1}$). The increased damping of the redshift-space power spectrum on small scales is a generic feature of $f(R)$ gravity. This is because the fifth force causes the particles to move faster, i.e. with a larger velocity dispersion than they do in GR for the same mass structure.

In Fig. 4 we also compare the measured ratios from two different simulation boxes of $L_{\mathrm{box}} = 1000\,\mathrm{Mpc}\,h^{-1}$ (circles) and $L_{\mathrm{box}} = 1500\,\mathrm{Mpc}\,h^{-1}$ (dashed lines) on a side. Each simulation has the same number of particles, 1024^3, but with different resolutions. In the $L_{\mathrm{box}} = 1500\,\mathrm{Mpc}\,h^{-1}$ simulation, the domain grid[2] has 1024^3 cells with a refinement criterion equal to nine particles (which means that a cell is refined into eight 'son' cells if the number of particles inside it exceeds nine). The $L_{\mathrm{box}} = 1000\,\mathrm{Mpc}\,h^{-1}$ simulation was run with the same domain grid and refinement criterion. As a result, both the mass and force resolutions are higher in the $L_{\mathrm{box}} = 1000\,\mathrm{Mpc}\,h^{-1}$ simulation. The force resolution is 15.3 and $22.9\,\mathrm{kpc}\,h^{-1}$ in the 1 and $1.5\,\mathrm{Gpc}\,h^{-1}$ box simulations, respectively. This can be compared to the force resolution of $781\,\mathrm{kpc}\,h^{-1}$ for the $400\,\mathrm{Mpc}\,h^{-1}$ box and $125\,\mathrm{kpc}\,h^{-1}$ for the $64\,\mathrm{Mpc}\,h^{-1}$ box used by Schmidt et al. (2009a). In Fig. 4 the higher resolution simulation shows more damping on small scales, and this is clearly seen in the quadrupole-to-monopole moment ratio plotted in the right-hand panel. This difference in the results from different computational boxes shows that large-volume high-resolution simulations are essential in order to accurately resolve the velocity field on scales $k > 0.3\,h\,\mathrm{Mpc}^{-1}$ and provide accurate predictions for the power spectrum in redshift space. In this paper we restrict our study to scales $k < 0.3\,h\,\mathrm{Mpc}^{-1}$ where the velocity field is accurately resolved in both simulations. We will only show results from the $L_{\mathrm{box}} = 1500\,\mathrm{Mpc}\,h^{-1}$ simulation in the rest of the paper unless otherwise stated.

In Fig. 5 we plot the ratio of the quadrupole to monopole moment of the redshift-space power spectrum at $z = 0$ measured in the F5 (left-hand panel) and F6 simulations (right-hand panel) along with the measured ratios in GR. The fifth force is more strongly suppressed in both of these models compared to the F4 model. As a result we find no detectable boost in the power spectrum on large scales compared to GR and less damping on small scales compared to F4. The F5 model in the left-hand panel of Fig. 5 still shows significantly more damping on small scales compared to GR, whereas the difference between the F6 model and GR at $z = 0$ is very small even down to small scales ($k \sim 0.3\,h\,\mathrm{Mpc}^{-1}$). This implies that the particles inside haloes are not significantly affected by the fifth force in the F6 model, while in F5 they have started to feel an effect.

Fig. 6 shows how the quadrupole-to-monopole moment ratios of the redshift-space power spectrum for GR and the F4 model change with redshift. The lower (upper) panel shows the measured ratios at $z = 0.4$ ($z = 1.0$), together with the linear theory predictions for each model (red dotted line for GR and green dot–dashed line for F4) at the same redshift. We can clearly see that the linear theory predictions agree with the measured ratios on slightly smaller scales (down to $k \sim 0.05\,h\,\mathrm{Mpc}^{-1}$) at $z = 1$ than at $z = 0$ for both models, as expected. The ratio P_2/P_0 in the F4 models is slightly larger than GR on large scales, but it suffers stronger damping on small scales compared to GR, such that the ratio becomes smaller than GR on non-linear scales. This large-scale boost of the power

---

[2] Here the domain grid is the finest grid that is uniform across the computational box.

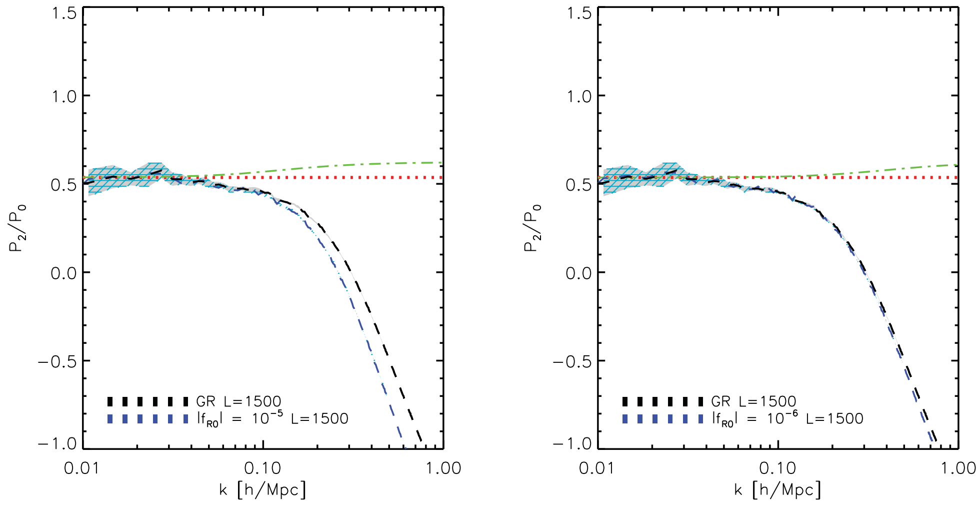

Figure 5. Left-hand panel: the ratio of the quadrupole to monopole moment of the redshift-space power spectrum at $z = 0$ in the F5 (blue) and GR (black) cosmologies. Right-hand panel: the same ratio of the quadrupole to monopole moment of the redshift-space power spectrum at $z = 0$ in the F6 (blue) and GR (black) cosmologies. The linear theory prediction for each model is shown as a green dot–dashed line for the $f(R)$ model and as a red dashed line for GR. The shaded regions represent the errors on the ratios measured from six simulations of the $f(R)$ (blue hatched) and GR (grey solid) cosmologies. The simulation box size used was $L_{\rm box} = 1500\,{\rm Mpc}\,h^{-1}$ on a side.

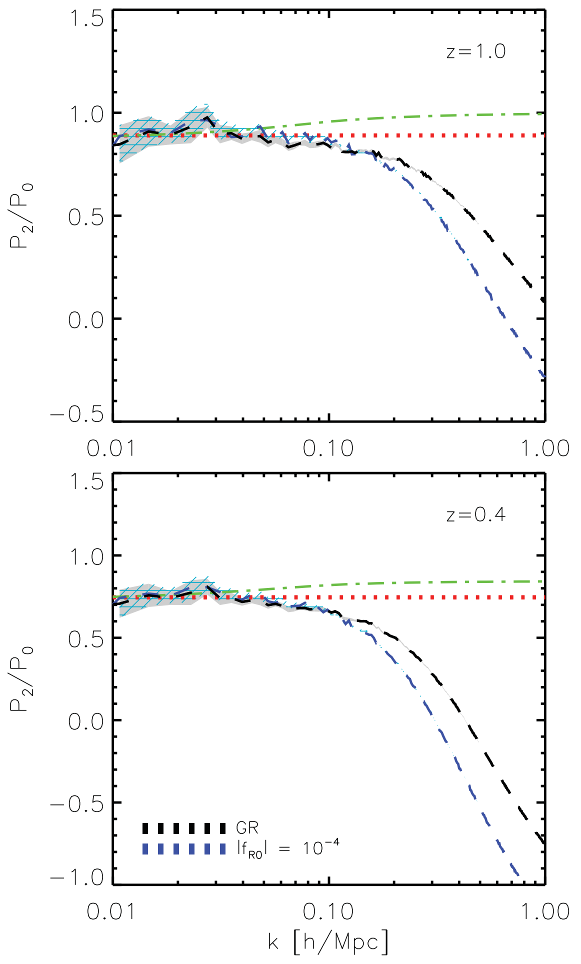

Figure 6. The ratio of the quadrupole to monopole moment of the redshift-space power spectrum for ΛCDM and the F4 model at $z = 0.4$ (bottom panel) and $z = 1$ (top panel). The linear theory prediction at each redshift is shown as a green dot–dashed line for the $f(R)$ model and as a red dashed line for GR.

spectrum and extra small-scale damping compared to GR are more pronounced at higher redshifts, which seems to contradict the naive expectation given that the fifth force is weaker then. This is because the fifth force effect has already been felt well before $z = 1$ as the screening is weaker at these epochs, after which the GR result slightly catches up and so the difference from F4 is reduced. Indeed, the same trend can also be seen in the linear perturbation results plotted in this figure.

Fig. 7 shows the ratio of P_2/P_0 in the F4 models to that in GR at $z = 0$, 0.4 and 1 measured from the simulations, together with the linear theory predictions. Linear theory predicts that the relative difference of P_2/P_0 between F4 and GR is larger at lower redshifts as expected. However, the relative difference measured in simulations on large scales is smaller at lower redshifts. This is due to the extra damping in the F4 models. This damping becomes stronger at lower redshifts and overcomes the linear enhancement of P_2/P_0 in the F4 models.

The strong enhancement in the small-scale damping in the F4 and F5 models compared to that in GR, which we have seen above, could be a clear signal of modified gravity that persists at higher redshifts. Of course, here we are only talking about the dark matter power spectrum and, as discussed in Section 3.2, models for the redshift-space power spectrum on small scales need to account for non-linear bias effects. As this is most relevant when studying the clustering of haloes in redshift space, we leave this analysis to future work.

4.2 The velocity power spectrum

The non-linear evolution of velocity fields on large scales can have a significant impact on the redshift-space power spectrum. Scoccimarro (2004) showed that the velocity field is more sensitive to tidal gravitational fields compared to the density field on large scales. Taking these non-linear velocity effects into account results in an improved model for the power spectrum in redshift space in the quasi-linear regime (Jennings et al. 2011a).

Measuring the velocity power spectrum from simulations can be difficult. The method suggested by Scoccimarro (2004) allows a

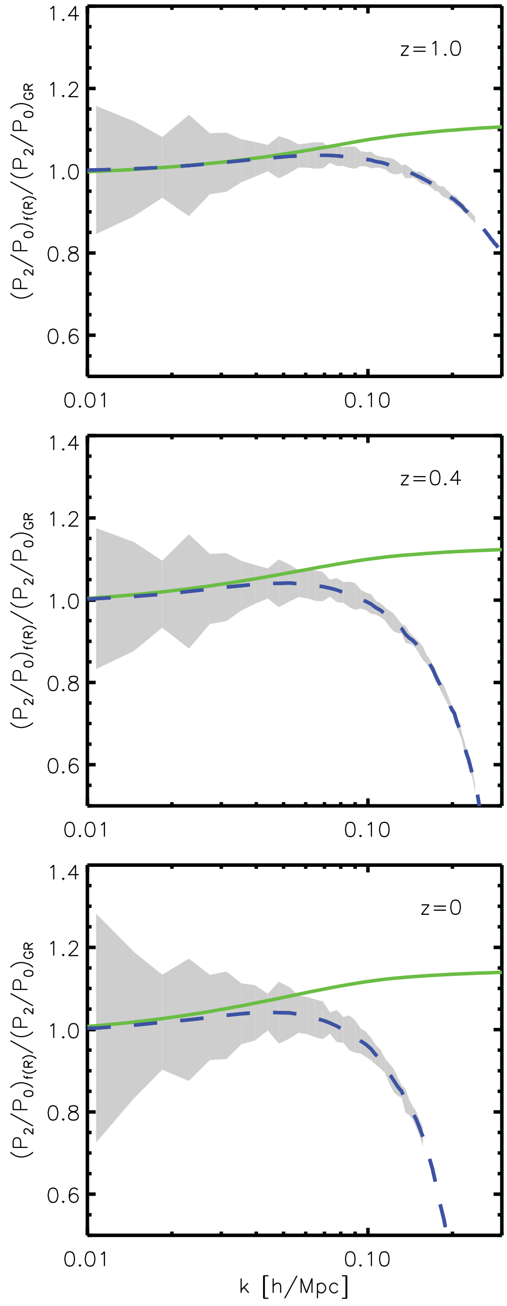

Figure 7. The ratio of P_2/P_0 in the F4 model to that in GR at $z = 0$ (bottom panel), $z = 0.4$ (middle panel) and $z = 1$ (top panel) measured from the simulations. The linear theory prediction for this ratio at each redshift is shown as a solid green line.

mass-weighted velocity field to be constructed but is limited by the fact that it is the momentum field which is calculated on a grid and so the velocity field in empty cells is artificially set to zero (Pueblas & Scoccimarro 2009). Another limitation of this method is that most calculations require the volume-weighted velocity field instead of the mass-weighted field. Using a Delaunay tessellation of a discrete set of points allows the desired volume-weighted velocity field to be constructed accurately on small scales. We use the publicly available DTFE code (Schaap & van de Weygaert 2000; van de Weygaert & Schaap 2009; Cantun & van de Weygaert 2011) to construct the velocity divergence field directly. This code constructs the Delaunay tessellation from a discrete set of points and interpolates the field values on to a user-defined grid. For the $L_{\rm box} = 1500\,{\rm Mpc}\,h^{-1}$ simulation we are able to generate the velocity auto, $P_{\theta\theta}$, and cross-power spectrum, $P_{\delta\theta}$, on a 1024^3 grid. The density field is interpolated on to the grid using the cloud-in-cell scheme. The resolution of the mesh means that mass assignment effects are negligible on the scales of interest here.

Fig. 8 shows the $z = 0$ non-linear velocity and matter power spectra measured from the F4 (left-hand panels) and GR (right-hand panels) simulations. The errors calculated from the scatter amongst six simulations are shown as a hatched region for the cross-power spectrum, $P_{\delta\theta}$, and as a solid shaded region for the autopower spectrum, $P_{\theta\theta}$. We show the velocity power spectrum from both the $L_{\rm box} = 1500\,{\rm Mpc}\,h^{-1}$ (dashed lines) and $L_{\rm box} = 1000\,{\rm Mpc}\,h^{-1}$ (circles) simulations. The lower panel in each case shows the ratio of $P_{\theta\theta}/P_{\delta\delta}f^2$ and $P_{\delta\theta}/P_{\delta\delta}f$ for each model. The scales where the linear continuity equation breaks down are shown by the departure of the measured ratios from unity. This occurs on slightly larger scales for GR than for the $f(R)$ model. The fact that the velocity power spectrum departs from linear theory on larger scales than the density field agrees with what has been noted previously by Scoccimarro (2004) and Jennings et al. (2011a). We find that $P_{\delta\delta}$ and $P_{\theta\theta}$ differ to 20 per cent at $k < 0.1\,h\,{\rm Mpc}^{-1}$.

When the velocity power spectrum is normalized using the linear growth rate as in Fig. 8, the ratios of the non-linear velocity and matter power spectra look very similar in both the standard and the modified gravity cosmologies. If instead we choose not to normalize θ using the growth rate, we get the curves shown in the top row of Fig. 9 for the ratio $\sqrt{P_{\theta\theta}/P_{\delta\delta}}$ (left-hand panel) and $P_{\delta\theta}/P_{\delta\delta}$ (right-hand panel) for the F4 and ΛCDM cosmologies. Note that in linear perturbation theory these two ratios equal the linear growth rate, f, which is plotted as a solid green line for the $f(R)$ model and as a dotted black line for ΛCDM in Fig. 9. There is clearly a large difference in the amplitude and shape of these ratios in the two models on scales $k > 0.03\,h\,{\rm Mpc}^{-1}$. It is interesting that the ratios agree with the predictions for the linear growth rate on scales where the two models can be distinguished within the errors, shown by the hatched shaded region for $f(R)$ and solid shaded region for ΛCDM. This is in contrast to the multipole moments of the redshift-space power spectrum, Fig. 4, where the Kaiser model predictions using the linear growth rate only agree with the measured $P(k)$ on extremely large scales where the two cosmologies could not be distinguished within the errors. The linear growth rate for the F4 model differs from that in ΛCDM by up to 20 per cent for $k < 0.1\,h\,{\rm Mpc}^{-1}$ (see Fig. 1).

In the middle and bottom rows of Fig. 9 we plot similar ratios for the F5 and F6 models, respectively. For these two models the difference in the ratios compared to ΛCDM is less dramatic than for the F4 model. This is to be expected as the linear growth rate for these models only differs from that in ΛCDM by at most 6 per cent for F5 and ~1 per cent for F6 on scales $k < 0.1\,h\,{\rm Mpc}^{-1}$. Furthermore, the simulation results start to deviate from the linear perturbation prediction earlier than it does for the F4 model. This is because the suppression of the fifth force itself is a non-linear effect and the non-linearity gets weaker as $|f_{R0}|$ increases, making the linear perturbation a better approximation for F4.

Fig. 10 shows the redshift evolution of the ratio $\sqrt{P_{\theta\theta}/P_{\delta\delta}} = f$ for the GR (black dotted line for linear perturbation prediction and blue dashed line measured from N-body simulation) and F4 model (green solid and purple dashed lines, respectively) at $z = 0.4$ (lower panel) and $z = 1$ (upper panel). The absolute difference in this ratio for these the two models is even more pronounced at higher redshift,

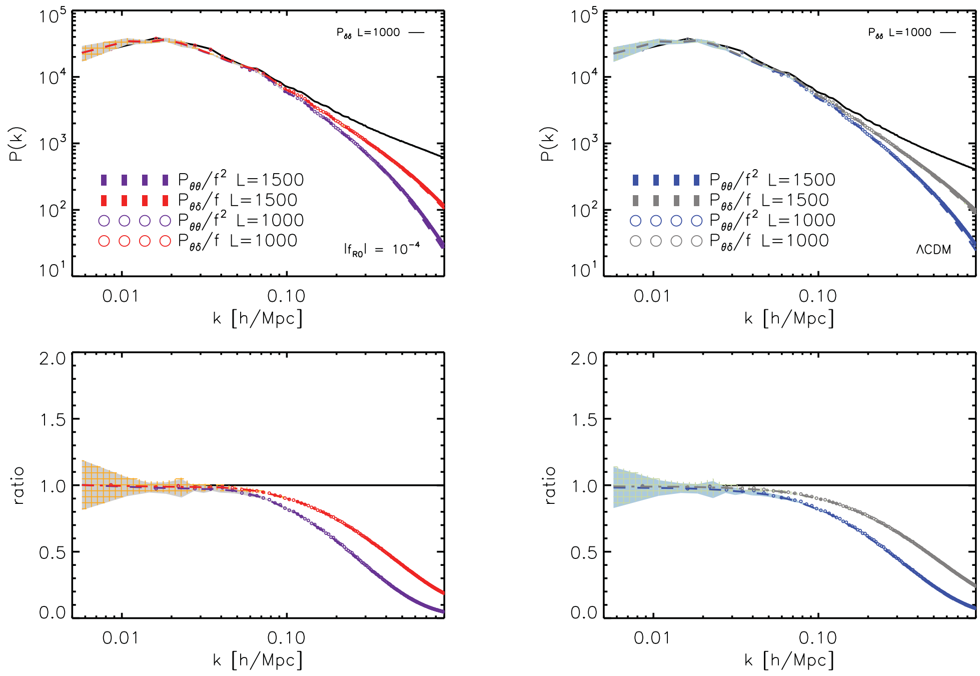

Figure 8. Left-hand panel: the velocity divergence autopower spectrum $P_{\theta\theta}/f^2$ (purple) and cross-power spectrum $P_{\delta\theta}/f$ (red) at $z = 0$ measured from the F4 model simulation. The lower ratio plot shows $P_{\theta\theta}/P_{\delta\delta}f^2$ (purple) and $P_{\delta\theta}/P_{\delta\delta}f$ (red). Right-hand panel: the velocity divergence autopower spectrum $P_{\theta\theta}/f^2$ (blue) and cross-power spectrum $P_{\delta\theta}/f$ (grey) at $z = 0$ measured from the ΛCDM simulation. The lower ratio plot shows $P_{\theta\theta}/P_{\delta\delta}f^2$ (blue) and $P_{\delta\theta}/P_{\delta\delta}f$ (grey). The non-linear matter power spectrum is plotted as a solid black line for each model. The measured $P(k)$ from the $L_{\rm box} = 1500$ and $1000\,{\rm Mpc}\,h^{-1}$ simulations are plotted as dashed lines and circles, respectively.

for the same reason as discussed in the redshift evolution of P_2/P_0 (Fig. 6).

The measured ratio agrees with the linear theory predictions for the growth rate on scales $k < 0.07\,h\,{\rm Mpc}^{-1}$ for the $f(R)$ model and $k < 0.04\,h\,{\rm Mpc}^{-1}$ for ΛCDM at $z = 1$, which is again as expected because linear perturbation is a better approximation at earlier times.

Fig. 11 shows the ratio of f in F4 to that in GR at three different redshifts. We also plot the linear theory prediction for the ratio $f_{f(R)}/f_{\rm GR}$ as a green solid line in this figure. Linear perturbation theory predicts that the ratio becomes larger at lower redshifts, which is shown by a small increase in the green line in Fig. 11 at $k \sim 1\,h\,{\rm Mpc}^{-1}$. On the other hand, the ratio $f_{f(R)}/f_{\rm GR}$ obtained from the simulations remains roughly the same at $k < 0.2\,h\,{\rm Mpc}^{-1}$ at all three redshifts and decreases at increasing redshift on smaller scales due to increased damping in the F4 model compared to GR. The fractional difference is ~12 per cent where the growth rate in F4 models peaks and the onset of the increase occurs on scales of $k \sim 0.2, 0.15$ and $0.09\,h\,{\rm Mpc}^{-1}$ for $z = 1, 0.4$ and 0, respectively. This is because the damping of the velocity power spectrum due to non-linearity becomes larger at lower redshifts on small scales, compensating the enhancement on large scales. The shift of the onset of the peak towards larger scales at later times merely reflects the fact that small scales are affected earlier.

4.3 Extracting the matter and velocity power spectra

In this section we investigate if a model for the 2D redshift-space power spectrum can be used to extract the density and velocity power spectra, as a function of scale, at $k < 0.1\,h\,{\rm Mpc}^{-1}$. If we were able to measure both of these power spectra accurately, this would provide us with a measure of the growth rate of structure, as seen in Fig. 9, which may be scale-dependent as is the case for the $f(R)$ gravity model. The motivation for restricting ourselves to these large scales, $k < 0.1\,h\,{\rm Mpc}^{-1}$, is that the impact of bias and non-linear damping due to velocity dispersions is expected to be small over this range (see e.g. Angulo et al. 2008).

The left- and right-hand panels in Fig. 12 show the 2D power spectrum for GR and the F4 model, respectively, plotted as a function of wavenumber k and μ at $z = 0$. The coloured shading represents the values of $\log_{10}P(k,\,\mu)$ measured from the simulations. The overplotted red lines represent the model of equation (25) which uses the velocity and density power spectra measured from each simulation. From both of these plots, it appears that the amplitude predicted by the model in equation (25) agrees with the measured 2D spectra although it fails to capture the detailed shape of the 2D spectrum over the full range of k and μ. This result agrees with what was found by Kwan, Lewis & Linder (2012).

In order to test the precision with which the model in equation (25) can reproduce the 2D power spectrum, we shall fit for both the velocity, $P_{\theta\theta}$, and matter power spectra, $P_{\delta\delta}$, under the assumption that in the quasi-linear regime $P_{\delta\theta} = \sqrt{P_{\theta\theta}P_{\delta\delta}}$ (Percival & White 2009). We have verified that this is true for our simulations to within a few per cent accuracy for $k < 0.1\,h\,{\rm Mpc}^{-1}$. We perform this fit over separate k bins of width $\Delta k = 0.01\,h\,{\rm Mpc}^{-1}$ up to a maximum of $k = 0.1\,h\,{\rm Mpc}^{-1}$, using the entire range of $0 < \mu < 1$.

The results of fitting to the F4 simulation at $z = 0$ and 1 are shown in the left- and right-hand panels, respectively, in Fig. 13. The average power spectra, $P_{\theta\theta}$ (lower curves) and $P_{\delta\delta}$ (upper curves), measured from the six simulations are plotted as a black dashed line for ΛCDM and a solid purple line for the $f(R)$ model at each redshift. The red filled circles show the results of the fit for each power spectrum measured from the F4 simulation. At $z = 0$ we show the result of the fit for each power spectrum measured from the GR simulation as green squares. At both redshifts it is clear

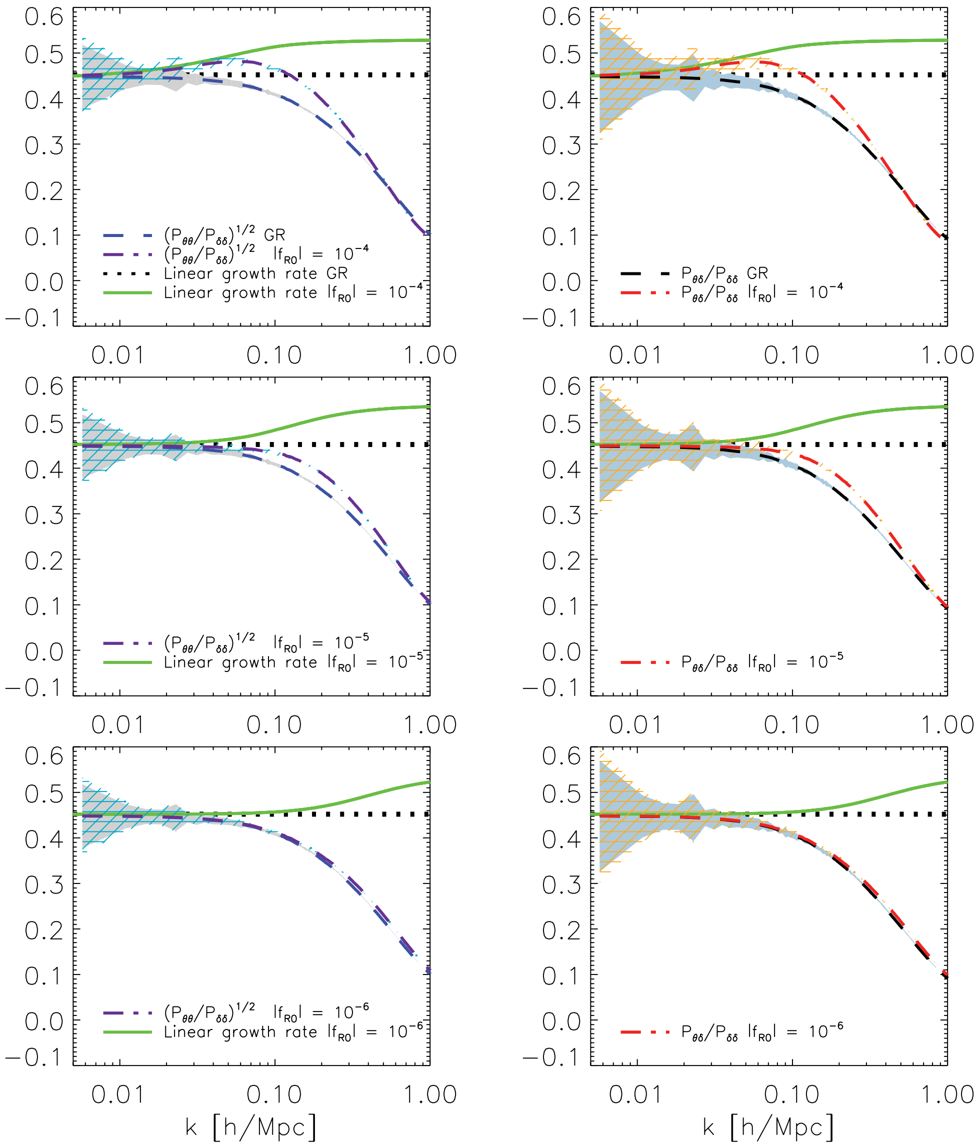

Figure 9. Top left-hand panel: the ratio $\sqrt{P_{\theta\theta}/P_{\delta\delta}}$ at $z = 0$ for the F4 (dashed purple) and ΛCDM (dashed blue) models. The same ratio is shown for F5 and F6 models in the middle and bottom left-hand panels, respectively. Top right-hand panel: the ratio $P_{\delta\theta}/P_{\delta\delta}$ at $z = 0$ for the F4 (dashed red) and ΛCDM (dashed black) models. The same ratio is shown for F5 and F6 in the middle and bottom right-hand panels, respectively. In all panels the variable $\theta = \nabla \cdot \boldsymbol{u}$. The errors for the $f(R)$ model are shown as hatched shaded regions and as solid shaded regions for ΛCDM. The linear growth rate is plotted as a solid green line and as a dashed black line for each $f(R)$ model and ΛCDM, respectively.

that the model in equation (25) is able to accurately describe the amplitude of the 2D $P(k, \mu)$. The matter power spectrum, $P_{\delta\delta}$, is recovered accurately and is distinguishable from ΛCDM. Unfortunately, this model is not able to reproduce the velocity power spectra from the modified gravity model and at both redshifts is biased to lower values. We have verified that fitting equation (25) over a reduced range in μ allows us to recover the correct $P_{\theta\theta}$, but at the cost of an increase in the errors by more than the difference in the two cosmologies. These results demonstrate that the redshift-space distortion model, $P(k, \mu) = P_{\delta\delta}(k) + 2\mu^2\sqrt{P_{\theta\theta}P_{\delta\delta}} + \mu^4 P_{\theta\theta}(k)$, accurately describes the amplitude of the 2D power spectrum and can recover $P_{\delta\delta}$, but the angular dependence on μ is incorrect and so we cannot extract $P_{\theta\theta}$. These results are in agreement with work by Tang, Kayo & Takada (2011). These authors fit for the density velocity cross-power spectrum $P_{\delta\theta}$ and find a similar bias in recovering the velocity power spectrum using this model. We have also fitted the model in equation (23), allowing the velocity dispersion damping term to be a free parameter. This method recovers the correct $P_{\theta\theta}$ within the error bars, but the constraints on the velocity power spectra are too weak to distinguish between GR and the F4 model. This measurement of $P_{\theta\theta}$ would not be accurate enough to allow us to discriminate between the F4 model and ΛCDM at either redshift.

4.4 Modelling the moments of the redshift space *P*(*k*)

In this section we return to studying the moments of the redshift-space power spectrum, P_0 and P_2. As shown in Section 4.3, the model given in equation (25) fails to capture the shape of the full 2D $P(k, \mu)$, so naively we do not expect that we can precisely measure these moments on all scales. In this section we investigate how well this model works at recovering the measured moments on

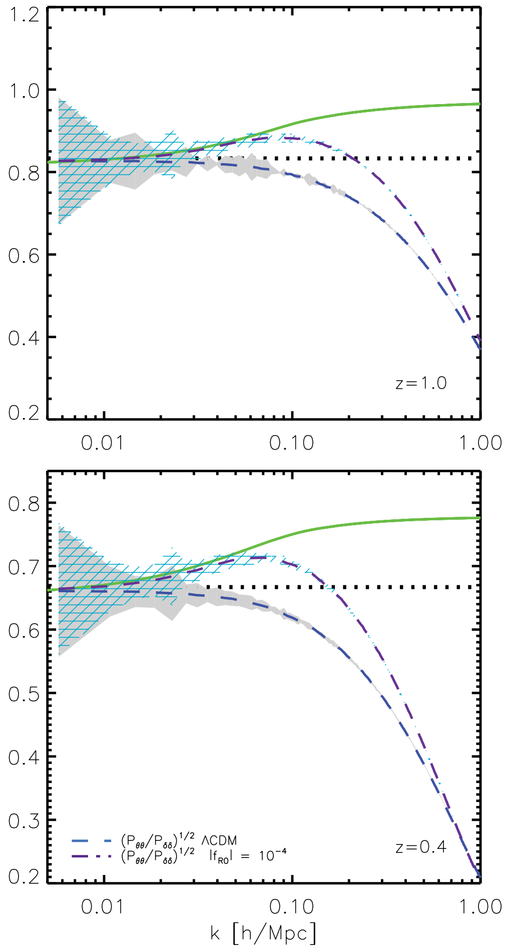

Figure 10. The ratio $\sqrt{P_{\theta\theta}/P_{\delta\delta}}$ at $z = 0.4$ (lower panel) and $z = 1$ (upper panel) for the F4 (dashed purple) and ΛCDM (dashed blue) models. The linear growth rate at each redshift is plotted as a solid green line and a dashed black line for the $f(R)$ model and ΛCDM, respectively.

large scales after averaging over μ. Previous work has shown that the model given in equation (26) provides a good fit to measurements from simulations on quasi-linear scales $k < 0.3\,h\,\mathrm{Mpc}^{-1}$ and at high redshifts $z \approx 1$, without the need to include a damping term (Jennings et al. 2011a).

The $z = 1$ multipole moments, P_0 (upper curves) and P_2 (lower curves), measured from the ΛCDM (empty black squares) and F4 (filled purple circles) simulations are shown in Fig. 14. These two power spectra have been separated in this plot for clarity. The model given in equation (26) using the velocity and matter power spectra from the simulations are overplotted as a green dot–dashed line and a red dotted line for the $f(R)$ and the ΛCDM cosmologies, respectively. The inset panel shows the ratio of the measured P_0 to the model for each cosmology, F4 (green dot–dashed lines) and ΛCDM (red dotted lines). The model for the monopole moment reproduces the measurement for the $f(R)$ model to within 10 per cent accuracy at $k < 0.2\,h\,\mathrm{Mpc}^{-1}$. The P_0 model for ΛCDM is accurate to within 5 per cent at $k < 0.2\,h\,\mathrm{Mpc}^{-1}$. The solid black line in the inset panel shows the ratio of the monopole moment in the F4 model to ΛCDM. The model precision for ΛCDM is sufficient to detect the 15 per cent difference in the monopole moment which we find between the two cosmologies on these large scales. The model in equation (26) requires accurate knowledge of the velocity and matter power spectra as input parameters. In this section we have used $P_{\theta\theta}$ and $P_{\delta\delta}$ measured from the simulations. An alternative to this would be to use fitting formula for each of these power spectra which have sufficient accuracy on these large scales (see e.g. Smith et al. 2003; Jennings et al. 2011a).

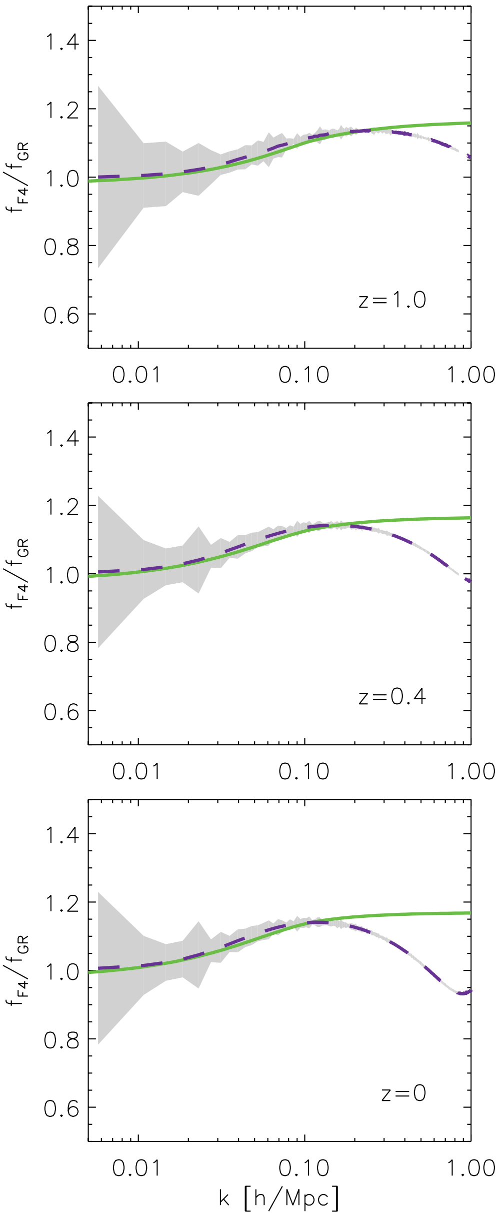

Figure 11. The ratio $f_{\mathrm{F4}}/f_{\mathrm{GR}}$ where $f = \sqrt{P_{\theta\theta}/P_{\delta\delta}}$ at $z = 0$ (bottom panel), $z = 0.4$ (middle panel) and $z = 1.0$ (top panel) in the F4 model compared to GR (purple dashed lines). The linear theory prediction for this ratio at each redshift is shown as a solid green line.

5 SUMMARY AND CONCLUSIONS

Modified gravity theories generally predict different clustering properties of matter, and as a result both the density and the velocity power spectra could be very different from the predictions of GR. The $f(R)$ gravity model has been a leading example of this in recent years. Here, the enhancement to the standard gravity depends sensitively on the local matter density through the so-called chameleon mechanism. In high matter density and high-curvature regions ($f_R \ll |\Phi|$, where Φ is the Newtonian potential), the

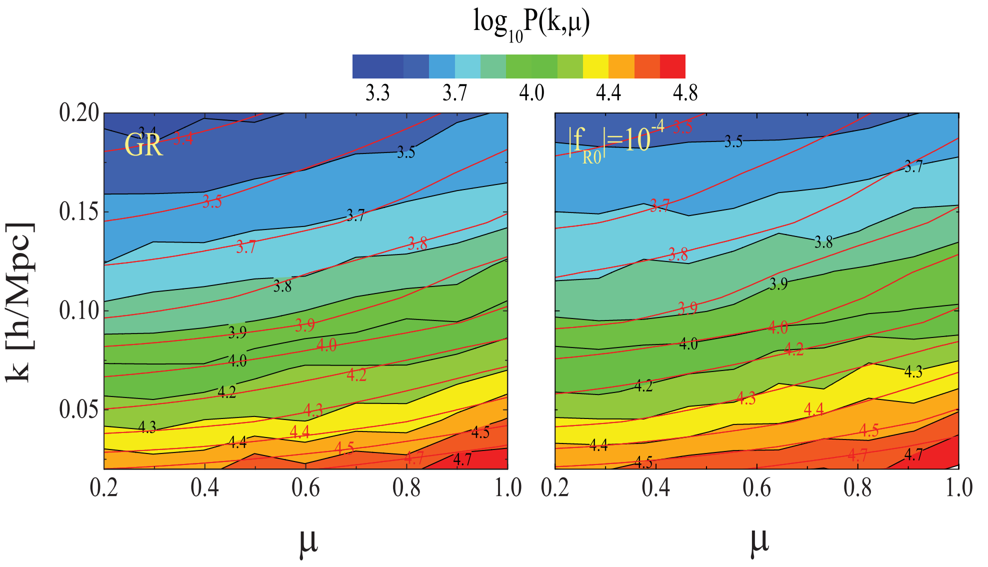

Figure 12. The 2D redshift-space power spectrum, $P(k, \mu)$, measured from the ΛCDM simulation (left-hand panel) and the F4 simulation (right-hand panel) at $z = 0$. The coloured contours and black solid lines represent $\log_{10}P(k, \mu)$. The overplotted red solid lines show the predictions of the model of equation (25), where the matter and velocity power spectra used for each cosmology have been measured from the simulation.

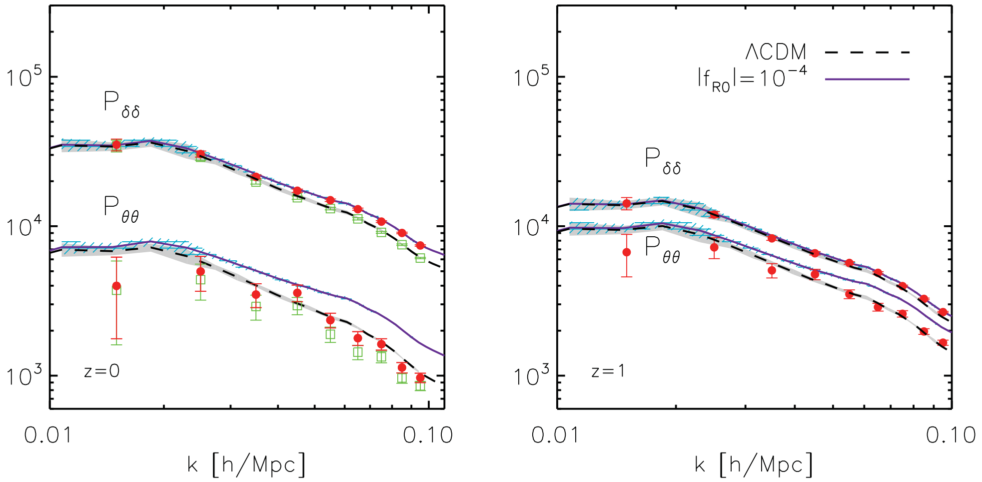

Figure 13. Left-hand panel: the non-linear matter (upper curves) and velocity (lower curves) power spectra measured from the $z = 0$ F4 (solid purple) and ΛCDM (dashed black) simulations. The filled red circles (green squares) show the results from fitting equation (25) to the 2D power spectrum, $P(k, \mu)$, from the F4 (GR) simulation. The error bars represent the 1σ errors on the fit; solid grey and hatched blue shaded regions represent the errors on the power spectrum measured from the ΛCDM and $f(R)$ simulations, respectively. Right-hand panel: same as the left-hand panel, but for $z = 1$.

enhancement is strongly suppressed and standard gravity is recovered; on the other hand, in low matter density and low-curvature regions the enhancement factor can be as large as 4/3. Depending on the value of f_{R0} and the local environment, the transition scale, or Compton length, of the scalaron ranges from less than one to more than a few megaparsecs, which can potentially leave detectable features in the distribution of matter and clustering patterns of the large-scale structure.

Galaxy surveys measure the distribution of matter in redshift space where the true position of a galaxy appears distorted along the line of sight due to peculiar velocities. The goal of many current and future galaxy redshift surveys is to constrain deviations from GR, and so it is important to understand how observables are affected by redshift-space distortions. Theoretical studies of this require both high-resolution and large-volume numerical simulations, which previously have not been performed for modified gravity models. In this paper we use simulations in large-volume boxes to carry out the first study of the clustering of the dark matter in redshift space in an $f(R)$ modified gravity. The simulation code developed by Li et al. (2012) allows us to model large volumes with good resolution.

The simulations we use in this analysis have two different resolutions, with 1024^3 dark matter particles in computational boxes of $L_{\rm box} = 1.5$ and $1.0\,h^{-1}$ Gpc on a side. We have checked that the simulations agree with one another down to $k \sim 0.3\,h\,{\rm Mpc}^{-1}$. We have compared the matter $P(k)$ measured in real space against previous simulations and found good agreement.

We have measured the redshift-space power spectrum in the GR and the $f(R)$ cosmologies at redshifts $z = 0, 0.4$ and 1. We find an enhanced boost in the power on large scales and a substantial increase in the damping on small scales in the $f(R)$ cosmology compared to GR at all redshifts. The deviations are largest for the

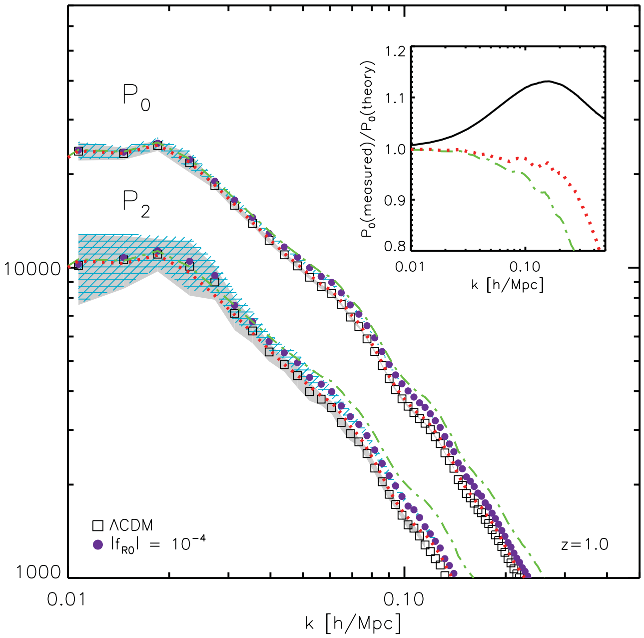

Figure 14. Upper curves: the monopole moment of the redshift-space power spectrum measured from the F4 (filled purple circles) and ΛCDM (empty black squares) simulations at $z = 1$. Lower curves: the quadrupole moment of the redshift-space power spectrum measured from the F4 (filled purple circles) and ΛCDM (empty black squares) simulations at $z = 1$. The two moments have been offset for clarity in this plot. The model in equation (25) for each power spectrum moment is shown as a dot–dashed green line for the $f(R)$ model and as a red dotted line for ΛCDM. The hatched (solid) shaded regions represent the errors on the measured power spectra for the $f(R)$ (ΛCDM) simulations. The inset panel shows the ratio of the monopole moment to the model in each cosmology, F4 (dot–dashed green lines) and ΛCDM (red dotted lines). The solid black line shows the ratio of the monopole moment in the F4 model to that in the ΛCDM model.

$f(R)$ model with parameter value $|f_{R0}| = 10^{-4}$ (F4) and are reduced as $|f_{R0}|$ is decreased. The large-scale enhancement of the power is a result of the fifth force in the modified gravity theory, which strengthens the matter clustering on large scales. On small scales where the local curvature is not too high, the fifth force makes the particles move faster, increasing the velocity dispersion and causing a stronger damping of the power compared to GR. These effects can be seen at various redshifts, and are even slightly stronger at earlier times. However, for some model parameters such as $|f_{R0}| = 10^{-6}$, the fifth force is strongly suppressed by the chameleon mechanism, and its effect is too weak to be distinguished from standard gravity. We find that the relative difference in the moments of the power spectrum, P_2/P_0, between the F4 $f(R)$ model and GR ranges from 20 per cent at $z = 1$ to 40 per cent at $z = 0$ at $k = 0.2\,h\,\mathrm{Mpc}^{-1}$ due to the enhanced non-linear damping on small scales.

We measure the velocity divergence power spectrum using the DTFE method in both $f(R)$ and GR cosmologies and find a large difference between $P_{\theta\theta}$ in the $f(R)$ model compared to GR. This difference is much larger than the difference between the non-linear matter $P(k)$ in the two models, suggesting that the velocity power spectrum is a far more sensitive probe of modified gravity. We find a large deviation in the ratios $\sqrt{P_{\theta\theta}/P_{\delta\delta}}$ and $P_{\delta\theta}/P_{\delta\delta}$ between the two models at $0.03 < k(\,h\,\mathrm{Mpc}^{-1}) < 0.5$ at $z = 0$. In linear theory these ratios equal the growth rate of structure, f, on large scales when the velocity divergence is normalized as $\theta = \nabla \cdot \boldsymbol{v}/aH$. Our results show that the measured ratios agree with the linear growth rate for each cosmology, which is scale-*dependent* in the case of modified gravity, for $k < 0.06\,h\,\mathrm{Mpc}^{-1}$ at $z = 0$. We find that the relative deviation of the measured non-linear ratio, $\sqrt{P_{\theta\theta}/P_{\delta\delta}}$, from the linear prediction between the $f(R)$ model and GR decreases with increasing redshift.

Using a simple quasi-linear model for the 2D redshift-space power spectrum, equation (25), which includes non-linear velocity terms but no small-scale damping parameter, we attempt to extract the matter and velocity power spectra. On scales $k < 0.1\,h\,\mathrm{Mpc}^{-1}$ we can recover the non-linear matter power spectrum to within a few per cent for both the $f(R)$ and the GR cosmologies. The model fails to describe the shape of the 2D power spectrum, and we are unable to reconstruct the velocity $P(k)$ accurately. The fact that this model recovers the non-linear matter power spectrum so precisely indicates that this method can be used to constrain modified gravity models. Our simulation results show that improved theoretical models are required in order to measure the velocity power spectrum where there is a large difference in the predicted signal between these two cosmologies.

We show that the same model works very well at fitting the first two multipole moments of the redshift-space power spectrum on large scales, especially at high redshifts. We are able to match the monopole moment to within 3 per cent for GR cosmology and 10 per cent for the $f(R)$ cosmology on scales $k < 0.2\,h\,\mathrm{Mpc}^{-1}$ at $z = 1$. This difference is smaller than the 15 per cent difference in the F4 and GR models on the same scales.

In this study we have addressed two separate questions. The first considers how well a simple model for redshift-space distortions, equation (25), works at recovering the non-linear matter and velocity $P(k)$ and how well it describes the multipole moments of the redshift-space power spectrum. The matter $P(k)$ and the monopole moment, P_0, are recovered accurately, and as a result we do not think that the failure of the model to describe the full 2D shape of $P(k, \mu)$ is a serious pitfall for future redshift-space analyses. Our results point to necessary adjustments needed in the model, such as including non-linear damping terms for example. Whether the velocity power spectrum can be extracted using more complicated modelling of the 2D power spectrum, and how well it can be measured, is left for future analysis. The second, two-part, question is: which observable, $P(k, \mu)$, P_0, P_2, etc., shows the largest difference between an $f(R)$ cosmology and a GR cosmology and is the simple redshift-space distortion model accurate enough to allow us to measure these differences? We observe the largest difference between these two cosmologies in the measured non-linear velocity power spectrum on scales $k > 0.03\,h\,\mathrm{Mpc}^{-1}$ and in the ratio of the multipole moments P_2/P_0 on scales $k > 0.2\,h\,\mathrm{Mpc}^{-1}$. Our results show that an improved model for redshift-space distortions is needed in order to extract the velocity power spectrum to a sufficient accuracy to distinguish an $f(R)$ cosmology from a GR cosmology. The differences between the ratios of the multipole moments, P_2/P_0, in GR and $f(R)$ are mainly on small scales. We shall address whether or not this difference is present in the redshift-space clustering of haloes and the effects of bias in future work.

To conclude, we find that redshift-space distortions in modified gravity models have an impact on the clustering of dark matter on large and small scales to a level which may be distinguished from GR. Current redshift-space distortion models, which are valid on quasi-linear scales, are accurate enough to extract the non-linear matter $P(k)$ in real space from the measured 2D redshift-space power spectrum on large scales, allowing us to constrain $f(R)$ modified gravity. The large difference between the predicted velocity $P(k)$ in the $f(R)$ and GR cosmology makes this a very promising observable with which to test GR provided that this can be accurately extracted from the redshift-space power spectrum. For certain $f(R)$ parameter values, e.g. $|f_{R0}| = 10^{-6}$, the impact of modified gravity on both the matter and velocity fields is not significant, and any deviations from GR are restricted to small scales. In a follow-up paper, we will examine the redshift-space distortions in the clustering of haloes in these modified gravity models on non-linear scales. We will test several non-linear models for redshift-space distortions to predict how well this observable can constrain $f(R)$ modified gravity in future surveys.

ACKNOWLEDGMENTS

EJ acknowledges the support of a grant from the Simons Foundation, award number 184549. This work was supported in part by the Kavli Institute for Cosmological Physics at the University of Chicago through grants NSF PHY-0114422 and NSF PHY-0551142 and an endowment from the Kavli Foundation and its founder Fred Kavli. BL is supported by the Royal Astronomical Society and Durham University. G-BZ and KK are supported by STFC grant ST/H002774/1. KK is thankful for support from the ERC and the Leverhulme Trust. The calculations for this paper were performed on the ICC Cosmology Machine, which is part of the DiRAC Facility jointly funded by STFC, the Large Facilities Capital Fund of BIS and Durham University. We thank Lydia Heck for technical support.

REFERENCES

Angulo R. E., Baugh C. M., Lacey C. G., 2008, MNRAS, 387, 921
Baugh C. M., Efstathiou G., 1994, MNRAS, 270, 183
Bertschinger E., Zukin P., 2008, Phys. Rev. D, 78, 2
Beutler F. et al., 2011, MNRAS, 416, 3017
Beutler F. et al., 2012, MNRAS, 416, 3017
Blake C. et al., 2010, MNRAS, 406, 803
Blake C. et al., 2011, MNRAS, 415, 2876
Blake C. et al., 2012, MNRAS, 425, 405
Brax P., van de Bruck C., Davis A. C., Shaw D. J., 2008, Phys. Rev. D, 78, 104021
Brax P., van de Bruck C., Davis A. C., Li B., Shaw D. J., 2011, Phys. Rev. D, 83, 104026
Brax P., Davis A. C., Li B., Winther H. A., 2012, Phys. Rev. D, preprint (arXiv:1203.4812)
Carroll S. M., Duvvuri V., Trodden M., Turner M. S., 2003, Phys. Rev. D, 70, 043528
Cautun M. C., van de Weygaert R., 2011, preprint (arXiv:1105.0370)
Cole S., Fisher K. B., Weinberg D. H., 1994, MNRAS, 267, 785
Davis A. C., Li B., Mota D. F., Winther H. A., 2012, ApJ, 748, 61
De Felice A., Tsujikawa S., 2010, Living Rev. Rel., 13, 3
Ferraro S., Schmidt F., Hu W., 2010, Phys. Rev. D, 83, 6
Gil-Marín H., Schmidt F., Hu W., Jimenez R., Verde L., 2011, J. Cosmol. Astropart. Phys., 11, 19
Green J. et al., 2011, Wide Field InfraRed Survey Telescope (WFIRST) Interim Report. ArXiv e-prints
Guzzo L. et al., 2008, Nat, 451, 541
Hamilton A. J. S., 1998, Astrophys. Space Sci. Library, 231, 185
Hu W., Sawicki I., 2007, Phys. Rev. D, 76, 064004
Jackson J., 1972, MNRAS, 156, 1P
Jennings E., Baugh C. M., Pascoli S., 2011a, MNRAS, 410, 2081
Jennings E., Baugh C. M., Pascoli S., 2011b, ApJ, 727, L9
Kaiser N., 1987, MNRAS, 227, 1
Khoury J., Weltman A., 2004, Phys. Rev. D, 69, 044206
Kwan J., Lewis G. F., Linder E. V., 2012, ApJ, 748, 78
Laureijs R. et al., 2011, Euclid Definition Study Report, preprint (arXiv:1110.3193)
Li B., Barrow J. D., 2007, Phys. Rev. D, 75, 084010
Li B., Barrow J. D., 2011, Phys. Rev. D, 83, 024007
Li Y., Hu W., 2011, Phys. Rev. D, 84, 084033
Li B., Zhao H., 2009, Phys. Rev. D, 80, 044027
Li B., Zhao H., 2010, Phys. Rev. D, 81, 104047
Li B., Zhao G., Teyssier R., Koyama K., 2012, J. Cosmol. Astropart. Phys., 1201, 051
Lombriser L., Slosar A., Seljak U., Hu W., 2010, preprint (arXiv:1003.3009)
LSST Science Collaborations, 2009, LSST Science Book, Version 2.0, preprint (arXiv:0912.0201), available at http://www.lsst.org/lsst/scibook
Marulli F., Baldi M., Moscardini L., 2012, MNRAS, 420, 2377
Matsubara T., 2008, Phys. Rev. D, 78, 083519
Mortonson M. J., Hu W., Huterer D., 2009, Phys. Rev. D, 79, 023004
Mota D. F., Shaw D. J., 2007, Phys. Rev. D, 75, 063501
Navarro I., Van Acoleyen K., 2007, J. Cosmol. Astropart. Phys., 02, 022
Nojiri S., Odintsov S. D., Phys. Rev. D, 68, 123512
Okumura T., Jing Y. P., 2011, ApJ, 726, 5
Oyaizu H., 2008, Phys. Rev. D, 78, 123523
Oyaizu H., Lima M., Hu W., 2008, Phys. Rev. D, 78, 123524
Peacock J. A., Dodds S. J., 1994, MNRAS, 267, 1020
Peacock J. A. et al., 2001, Nat, 410, 169
Peebles P. J. E., 1976, Ap&SS, 45, 3
Percival W. J., White M., 2009, MNRAS, 393, 297
Percival W. J. et al., 2007, MNRAS, 381, 1053
Pueblas S., Scoccimarro R., 2009, Phys. Rev. D, 80, 043504
Raccanelli A., Samushia L., Percival W. J., 2010, MNRAS, 409, 1525
Reid B. A., White M., 2011, MNRAS, 417, 1913
Reid B. A. et al., 2012, preprint (arXiv:1203.6641)
Samushia L., Percival W. J., Raccanelli A., 2012, MNRAS, 420, 2102
Sánchez A. G., Crocce M., Cabré A., Baugh C. M., Gaztañaga E., 2009, MNRAS, 400, 1643
Sánchez E. et al. (DES Collaboration), 2010, J. Phys. Conf. Ser., 259, 012080
Schaap W. E., van de Weygaert R., 2000, A&A, 363, L29
Schlegel D. J. et al., 2007, AAS, 38, 132
Schlegel D. J. et al., 2009, preprint (arXiv:0904.0468)
Schmidt F., 2009, Phys. Rev. D, 80, 043001
Schmidt F., Vikhlinin A., Hu W., 2009a, Phys. Rev. D, 8, 083505
Schmidt F., Lima M., Oyaizu H., Hu W., 2009b, Phys. Rev. D, 79, 083518
Scoccimarro R., 2004, Phys. Rev. D, 70, 083007
Scoccimarro R., Couchman H. M. P., Frieman J. A., 1999, ApJ, 517, 531
Seljak U., McDonald P., 2011, J. Cosmol. Astropart. Phys., 11, 39
Smith R. E. et al., 2003, MNRAS, 341, 1311
Sotiriou T. P., Faraoni V., 2010, Rev. Mod. Phys., 82, 451
Springel V., 2005, MNRAS, 364, 1105
Tang J., Kayo I., Takada M., 2011, MNRAS, 416, 2291
Taruya A., Nishimichi T., Saito S., 2010, Phys. Rev. D, 82, 063522
Teyssier R., 2002, A&A, 385, 337
van de Weygaert R., Schaap W., 2009, in Martnez V. J., Saar E., Martnez-Gonzalez E., Pons-Bordera M.-J., eds, Lecture Notes in Physics, Vol. 665, The Cosmic Web: Geometric Analysis. Springer-Verlag, Berlin, p. 291
Vanderveld R. A., Mortonson M. J., Hu W., Eifler T., 2012, Phys. Rev. D, 85, 103518
Weinberg D. H., Mortonson M. J., Eisenstein D. J., Hirata C., Riess A. G., Rozo E., 2012, preprint (arXiv:1201.2434)
Will C. M., 2006, Living Rev. Relativ., 9, 3
Yoshida N., Sheth R. K., Diaferio A., 2001, MNRAS, 328, 669
Zhao G., Li B., Koyama K., 2011, Phys. Rev. D, 83, 044007

This paper has been typeset from a TEX/LATEX file prepared by the author.